Journal of Materials Research and Technology 36 (2025) 7925–7949

Contents lists available at ScienceDirect

Journal of Materials Research and Technology

journal homepage: www.elsevier.com/locate/jmrt

Characterization and evaluation of joint properties of friction stir welded AA7075/GNPs joints obtained using square and cylindrical threaded tools

Rahul Biradar [a], Sachinkumar Patil [a,*], Nagamadhu M [b], Priyaranjan Sharma [c,**], Filipe Fernandes [d,e]

[a] School of Mechanical Engineering, REVA University, Bengaluru, Karnataka, 560064, India
[b] Department of Mechanical Engineering, BMS Institute of Technology & Management, Bengaluru, Karnataka, 560064, India
[c] Department of Mechanical Engineering, Manipal University Jaipur, Rajasthan, 303007, India
[d] University of Coimbra, CEMMPRE, ARISE, Department of Mechanical Engineering, Rua Luís Reis Santos, 3030-788, Coimbra, Portugal
[e] CIDEM, ISEP - Polytechnic of Porto, Rua Dr. António Bernardino de Almeida, 4249-015, Porto, Portugal

ARTICLE INFO

Handling editor: L Murr

Keywords:
Graphene nanoplatelets (GNPs)
Tool pin geometry
Electron back scatter diffraction (EBSD)
X-ray diffraction (XRD)
Transmission electron microscope (TEM)
Mechanical properties

ABSTRACT

This study investigates the joint properties and microstructural features of friction stir-welded (FSWed) AA7075 aluminum alloy composites reinforced with 1 wt % of graphene nanoplatelets (GNPs). It focuses on the influence of square (SQ) and cylindrical threaded (CT) tool pin geometries on material flow, GNPs dispersion, and weld quality. The authors conducted comprehensive evaluations using advanced characterization methods including scanning electron microscope (SEM), transmission electron microscope (TEM), X-ray diffraction (XRD), and Raman spectroscopy. The results reveal formation of precipitates and well bonding between aluminum alloy and GNPs, resulting in better quality of welds. The SQ tool facilitated superior material stirring and uniform dispersion of GNPs, leading to the formation of fine, equiaxed grains in the nugget zone (NZ). Electron back scatter diffraction (EBSD) analysis presents reduction of grain size of base material from 38 µm to 10 µm in the NZ, significantly enhancing mechanical properties. Welds produced using the SQ tool exhibited higher micro-hardness (150 HV) and tensile strength (630 MPa) compared to those made with the CT tool (141 HV and 478 MPa), resulting in a 75 % improvement in joint efficiency. Fracture analysis revealed ductile failure in the heat-affected zone (HAZ), with fine dimples observed in SEM images. Additionally, the SQ tool weld demonstrated a lower wear rate, reduced from 70 µm to 25 µm, than its counterpart. These findings highlight the importance of tool geometry in producing defect-free, high-performance welds.

1. Introduction

The AA7075 aluminum alloys are highly preferred in aerospace applications, including fuselage tanks and wing fabrication, due to their lightweight nature, superior corrosion resistance, and enhanced mechanical properties [1]. These attributes make them ideal for critical structural components where weight reduction is paramount. In the current manufacturing industry, there is a growing interest in advanced materials, particularly aluminum matrix composites (AMCs), owing to their enhanced properties. AMCs are fabricated using a variety of reinforcements, including silicon carbide (SiC), multiwalled carbon nanotubes (MWCNT), titanium carbide (TiC), alumina (Al_2O_3), boron carbide (B_4C), and graphite [2]. Studies have shown that aluminum alloys reinforced with nanoscale particles exhibit superior mechanical performance. Specifically, the integration of carbon-based nanomaterials has underscored the importance of evaluating the characteristics of carbon nanotubes (CNTs) and graphene nanoplatelets (GNPs) in AMCs for engineering uses [3,4]. Previous research has indicated that graphene serves effectively as a reinforcement in both polymer and ceramic matrices [5,6]. Its inclusion leads to notable improvements in tensile strength and hardness of the composites [7,8]. Furthermore, incorporating an optimal weight fraction of GNPs has been found to significantly enhance the strength of AMCs [9,10].

However, when AMCs are joined using traditional fusion welding techniques such as tungsten inert gas (TIG) and metal inert gas (MIG) welding, various defects—such as cracks, porosity, surface

---

* Corresponding author.
** Corresponding author.

E-mail addresses: sachinkumar.patil@reva.edu.in (S. Patil), priyaranjan.sharma@jaipur.manipal.edu (P. Sharma).

https://doi.org/10.1016/j.jmrt.2025.05.028
Received 26 March 2025; Received in revised form 4 May 2025; Accepted 5 May 2025

irregularities, and excessive flash—are commonly observed [11,12]. Also, the riveting processes used in aerospace manufacturing add considerable weight, thereby increasing fuel consumption. To address this, friction stir welding (FSW) emerges as a promising alternative, offering weight reduction while maintaining joint integrity. AA7075 alloys, composed of approximately 5.6 % zinc, exhibit exceptional corrosion resistance, making them suitable for demanding environments [13,14]. The aluminum/GNPs composites exhibited improved mechanical properties, including tensile strength, hardness, and tribological performance. The incorporation of GNPs in aluminum significantly reduced grain size and influenced grain misorientation, leading to increased tensile strength compared to the base alloy [15]. The grain refinement induced by graphene resulted from the combined effect of aluminum alloy/GNPs stimulated nucleation during DRX. Furthermore, the uniform distribution of GNPs reinforcements minimized grain boundary formation and restricted grain growth after recrystallization [16]. In contrast, FSW is a solid-state welding technique that produces superior joints through plastic deformation rather than complete material melting. The FSW process highlights the distinction between the advancing side (AS), where tool rotation and welding speed align, and the retreating side (RS), where they are opposite [17,18]. Severe plastic deformation during the FSW process leads to grain refinement and abnormal grain growth, which significantly impact the mechanical properties of the weld [19]. However, a higher welding speed combined with a constant rotational speed can cause void formation beneath the top surface of the weld on the AS of the nugget zone [20]. FSW performance depends heavily on parameters such as tool geometry, rotational and traverse speeds, axial force, plunge depth, tool offset, and tilt angle. The tilt angle, defined as the inclination of the tool axis relative to the workpiece surface, plays a pivotal role in achieving effective welding [21]. Additionally, the FSW process creates a circular arc on the surface due to the tool shoulder's rotation and translation, which serves as a potential crack initiation site in the welded specimen [22]. The FSW tool's design significantly influences heat generation, and the thermal cycle during the tool's plunge phase. This comprehensive understanding of FSW parameters and their impact underscores its potential to revolutionize aerospace manufacturing. Friction stir welded (FSWed) joints offer numerous advantages over fusion welding techniques, primarily due to the solid-state nature of the process, which avoids material melting and minimizes defects such as porosity and hot cracking [23,24].

FSW joints typically exhibit four distinct zones: base material (BM), thermo-mechanically affected zone (TMAZ), heat-affected zone (HAZ), and nugget zone (NZ), each characterized by unique microstructural and mechanical properties [25,26]. The tool pin profile plays a critical role in the FSW process, influencing material flow, heat input, and weld quality. Numerous studies have explored the impact of various tool pin designs on joint characteristics. Hasan et al. [27] investigated five tool profiles, including cylindrical taper, straight cylindrical, square, cylindrical threaded, and triangular, concluding that the square pin produces a homogeneous material distribution and superior ultimate tensile strength (UTS) of 303 MPa. Similarly, Elangovan et al. [28] and Amit et al. [29] observed enhanced microhardness and UTS in FSW joints processed with square pins, attributing the improvements to effective material stirring and grain refinement. Other researchers have highlighted the benefits of alternative pin profiles. Jayaseelan et al. [30] demonstrated superior grain refinement and reinforcement distribution using threaded cylindrical pins in aluminum alloy composites reinforced with SiC/ZrB_2. Krasnowski et al. [31] found that triflute pins yielded better mechanical properties in AA6082 alloys by promoting fine grain formation and minimizing dislocations in the NZ. Pankaj et al. [32] reported optimized heat generation and higher tensile strength in AA5052/Steel dissimilar joints using tapered cylindrical pins, while Rahul et al. [33] achieved homogenous Al_2O_3 dispersion and grain refinement in AA6061/Al_2O_3 joints using tapered cylindrical threaded pins. Mohsen et al. [34] observed a stable distribution of SiC particles and higher microhardness in AA7075/SiC composites welded using threaded tapered pins. Srinivasa et al. [35] reported improved joint efficiency (73.5 %) for AA65032 when welded with cylindrical tools. Yuqing et al. [36] found homogeneously dispersed η and η′ precipitate phases in the NZ of AA7075-T6 joints fabricated with conical taper tools, attributing these results to sufficient heat generation and intense mechanical mixing. Sivaraman et al. [37] studied the FSW of AA2014 and AA7075 alloys, achieved tensile strength of 160 MPa. Martin et al. [38] investigated the FSW of AA7075-T651, reporting defect-free welds with keyhole closure. Further, Navdeep et al. [39] examined the FSW of AA7075-T651/AlSi10Mg and found that the base material significantly influenced joint strength, with higher hardness observed in the NZ. Also, Hesam et al. [40] achieved a refined grain size of 40.2 nm during the friction stir processing (FSP) of Al-Cu-Mg alloy through enhanced cooling and grain growth control. Several recent studies have explored the influence of graphene nanoplatelets (GNPs) on the characteristics of friction stir welding (FSW) and FSP. Zhao et al. [41] conducted FSW on Al-Cu-Mg alloy reinforced with CNTs, achieving a joint efficiency of 87 %, attributed to the incorporation of CNTs. Abhishek et al. [42] performed FSW on AA6061/GNPs and observed improvements in weld strength and elongation by 121 % and 53 %, respectively. These enhancements were due to mechanisms such as grain refinement, load transfer, and Orowan looping. Zhang et al. [43] investigated the FSP of AA2009/GNPs composite and reported higher ultimate tensile strength (UTS) and yield strength (YS) values of 514 MPa and 398 MPa, respectively. The effective load transfer and high-strength efficiency were linked to the large specific surface area of uniformly distributed GNPs. Syahid et al. [44] examined FSW of a copper/AA6061 sheet incorporating 0.5 % graphene nanoparticles and found that the addition of graphene improved both strength and microhardness. Furthermore, Hesam et al. [45] noted that increasing the heat input during FSP of Al-Mg-Si/GNPs composites reduced the Zener-Hollomon parameter, leading to grain growth in the nugget zone (NZ). Pouraliakbar et al. [46] also reported that the FSP of AA6061 joints with dispersed GNPs resulted in enhanced UTS of 392 MPa, YS of 379 MPa, and microhardness improvement from 273 to 401 HV due to grain refinement.

The above literature survey provides a comprehensive understanding of the FSW process and its applications in joining aluminum alloys with various reinforcements. Despite significant progress in this field, certain gaps remain unaddressed. To the best of our knowledge, there is limited research on the incorporation of advanced reinforcements such as GNPs in AA7075 aluminum alloys have been reported so far. Furthermore, the comparative influence of different tool pin geometries on the microstructural, mechanical, and tribological properties of nanoparticle-reinforced FSW joints is yet to be fully explored. These gaps highlight the need for targeted investigations into the synergistic effects of advanced reinforcements and tool design parameters.

The novelty of this research lies in the exploration of GNPs as reinforcements in AA7075 aluminum alloys via FSW. This study uniquely investigates the comparative impact of SQ and CT tool pin geometries on microstructure, mechanical, and tribological properties of the GNPs-reinforced joints. The findings specifically highlight how SQ tools facilitate superior material stirring and uniform GNPs dispersion, leading to significant improvements in mechanical properties such as tensile strength, hardness, and wear resistance. This study fills gaps in the literature regarding the integration of advanced reinforcements like GNPs and highlights the role of tool design in optimizing joint quality for aerospace applications.

The incorporation of graphene nanoplatelets (GNPs) into an aluminum matrix has emerged as an innovative and transformative approach in materials engineering, particularly in the context of friction stir welding (FSW). This advancement leverages the exceptional mechanical and tribological properties of GNPs alongside the proven benefits of aluminum alloys, resulting in superior performance characteristics. The novelty of this development lies in both the choice of materials and the processing technique. FSW is particularly advantageous for fabricating composites, as it avoids common issues such as porosity, segregation, and degradation of reinforcement particles typically associated with traditional fusion welding methods. In FSW, a rotating tool generates frictional heat to plasticize the materials, facilitating the mixing and bonding of the composite constituents. When applied to aluminum/GNPs composites, FSW not only ensures effective joining but also promotes a refined microstructure and uniform dispersion of GNPs within the stirred zone.

2. Materials and methods

For the experimentation, the AA7075 base alloy was sourced from Fenfe Metallurgical Private Limited, Bengaluru, India. The AA7075 aluminum alloy known for its excellent mechanical strength and corrosion resistance, is employed as base material. The alloy composition predominantly contains Al-Zn-Mg-Cu, as detailed in Table 1, while its mechanical properties are outlined in Table 2. The alloy's high strength-to-weight ratio makes it an ideal candidate for aerospace and automotive applications. The GNPs were sourced from Adnano Technologies Private Limited, Shimoga, Karnataka, India. They have lateral dimensions of 10–12 μm and a thickness of 10–15 nm. These GNPs comprise multilayer graphene sheets with a platelet structure and a length of 1–5 μm. The GNPs renowned for their exceptional thermal and mechanical properties, are utilized as the reinforcement material to enhance the composite's overall performance. A detailed scanning electron microscope (SEM) image of GNPs are shown in Fig. 1((a) and (b)) at magnifications of 10 kx and 15 kx, provides insights into their morphology, with uniform distribution of GNPs in the aluminum matrix.

The AA7075/GNPs composites were fabricated using the stir casting technique. This method was applied with varying weight percentages of GNPs—0, 0.5, 1, and 1.5 wt%—to produce the AA7075/GNPs composites. Among these, the 1 wt% GNPs/7075 composite exhibited a uniform dispersion of GNPs, as shown in Fig. 1(c) and (d) at 500 × and 2000 × magnifications, respectively. The corresponding energy dispersive spectroscopy (EDS) analysis is presented in Fig. 1(e). Based on this observation, the 1 wt% GNPs/7075 composite was selected for friction stir welding and subsequent weld characterization. The stir casting process parameters used for composite fabrication are listed in Table 3.

The AA7075 ingots were heated to 800 °C in a crucible using an electric furnace. The required quantity of GNPs was preheated and then added to the molten aluminum, followed by stirring with a mechanical stirrer to ensure proper mixing. The resulting molten mixture was poured into a mild steel die maintained at room temperature. The stir-cast composite rectangular plates, measuring 190 mm × 70 mm × 6 mm (length × width × thickness), were then used for conducting FSW experiments. High-quality butt welds were produced using a state-of-the-art, custom-built 2-axis FSW machine (Make: ETA Technology Private Limited, Model: NI cRIO-9012), available at the Indian Institute of Science (IISc), Bengaluru, India. A schematic representation of the FSW process is shown in Fig. 2(a), while the clamping fixtures used for FSW are depicted in Fig. 2(b). The FSW tools used in this study—square (SQ) and cylindrical threaded (CT)—along with their dimensions, are illustrated in Fig. 2(c) and (d), respectively.

H13 tool steel, chosen for its excellent hardness and wear resistance, is used as the tool material and hardened to 52 HRC to withstand high temperatures and mechanical stress during welding. Table 4 presents the specifications of the FSW tools used. FSW experiments were performed by varying the tool rotational speed (TRS) from 700 rpm to 1400 rpm, while keeping the tool traverse speed (TTS) constant at 30 mm/min. At lower TRS values (700–1100 rpm), defects such as wormholes, tunnel defects, and cracks were observed, primarily due to insufficient heat input. On the other hand, TRS values above 1200 rpm resulted in pinholes and void defects, as shown in Fig. 3. Defect-free joints were achieved at a TRS of 1200 rpm, TTS of 30 mm/min, with a constant axial force of 4 kN and a tilt angle of 2°. Therefore, the main FSW experiments were conducted using these optimized process parameters.

Table 2
Mechanical properties of AA7075 alloy.

Ultimate tensile strength (MPa)	0.2 % offset yield stress (MPa)	Elongation (%)	Microhardness (HV)
156.5	108	1.6	125

Advanced characterization techniques were employed to analyze the joint properties, including a wear testing machine (Make: Ducom, Model: TR 20LE), tensile testing setup (Make: Biss nano 25 KN, Model: UT-01-0025), Vickers microhardness tester (Make: Wilson, Model: VH1102), and optical microscope (Make: Olympus, Model: BX53 M). The microstructure samples were polished using various grades of emery paper (100, 200, 300, and 400 μm), followed by alumina polishing with Al_2O_3 (1 μm size), diamond paste (¼ μm size), and diamond spray for a mirror finish. The polished samples were etched for 15 s in Keller's reagent (190 ml H_2O, 5 ml HNO_3, 3 ml HCl, 2 ml HF) to reveal surface morphologies [47]. The authors prepare the wear sample with ASTM G99 standard. Tensile test samples are prepared following ASTM E08-04 subsize standard, as illustrated in Fig. 4(a) and (b).

Microhardness samples were prepared following ASTM E384-11E1 for accuracy and repeatability. For each test, an average of three readings was taken for microhardness, tensile, and wear characterization. Electron backscatter diffraction (EBSD) analysis was performed using a Tescan MIRA 3 system. For EBSD sample preparation, electropolishing was conducted using A-2 solutions at 20 V, with a flow rate of 18 m^3/s for 18 s. Transmission electron microscopy (TEM) was carried out using a Titan Themis 300 kV FEI Thermo system, with specimens thinned to 60 nm using the focused ion beam (FIB) technique. X-ray diffraction (XRD) analysis was performed using a Rigaku Smart Lab system to determine the crystallographic structure. Raman spectroscopy was also conducted using a HORIBA Jobin Yvon LabRam HR system. All characterizations were conducted at room temperature. These tools and methodologies collectively enable a comprehensive evaluation of mechanical, microstructural, and tribological performance of AA7075/GNPs composites. Fig. 5 shows the flow chart of research methodology.

3. Results and discussion

3.1. Macrostructural observation

In fusion welding, aluminum alloys often form defects such as porosity, surface cracks, and slag inclusion, which compromise weld quality. These defects are primarily attributed to improper material flow and insufficient heat generation during the process [48]. In contrast, FSW offers a significant advantage as it eliminates such defects by operating in a solid state, joining metals through frictional heat, and continuous stirring action [27]. The cross-sectional views of FSWed joints, depicted in Fig. 6((a) and (b)) show the effect of material flow dynamics across the joint. The stable mixing and uniform distribution of plasticized material result from the combined action of the shoulder and pin flow. Fig. 6(a) displays a symmetric NZ along the weld line, extending from AS to RS. The NZ exhibits a recrystallized region with refined grains, while the TMAZ shows upward-stretched grains aligned

Table 1
Chemical composition of AA7075 alloy.

Zn	Mg	Mn	Cu	Si	Fe	Ti	Pb	Tn	Remaining
5.82	2.32	0.08	1.44	0.12	0.10	0.06	0.03	0.04	89.99

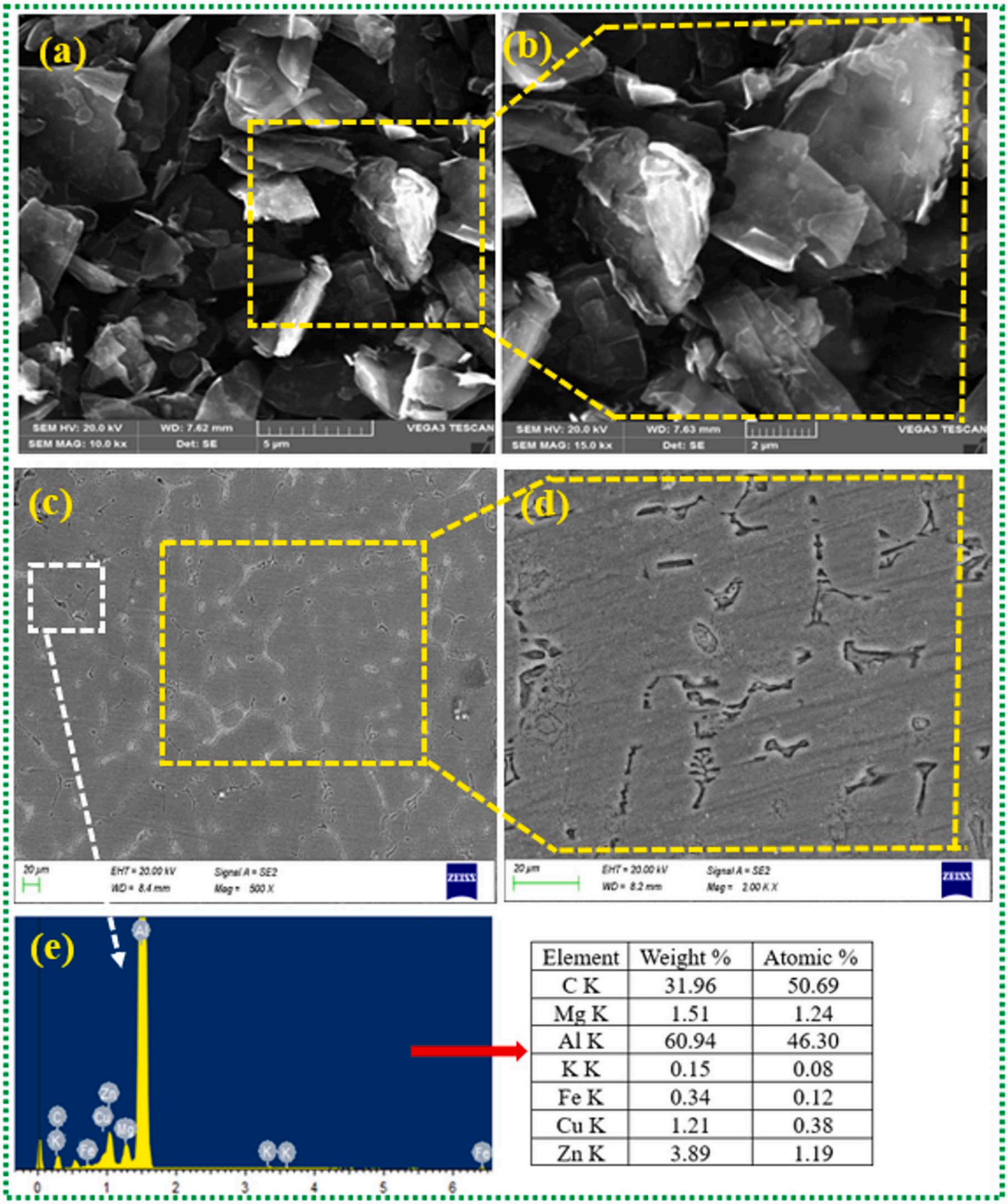

Element	Weight %	Atomic %
C K	31.96	50.69
Mg K	1.51	1.24
Al K	60.94	46.30
K K	0.15	0.08
Fe K	0.34	0.12
Cu K	1.21	0.38
Zn K	3.89	1.19

Fig. 1. SEM images of (a and b) GNPs at 10 Kx and 15 kx, (c and d) AA7075/1 wt% of GNPs at 500 x and 2 Kx, and (e) EDS of AA7075/1 wt % of GNPs.

Table 3
Stir casting process parameters.

Particulars	Details
Spindle speed	450 rpm
Stirring time	10 min
Preheated temperature of GNPs	40 °C
Preheat time	20 min
Preheating temperature of mould	200 °C
Reinforcement feed rate	1.0–1.5 g/s

with the material flow direction. In HAZ, the grain morphology remains largely unchanged, indicating minimal deformation.

In Fig. 6(b), the NZ exhibits asymmetry about the weld line, due to the CT tool's distinct material flow characteristics. On the AS, a sharp interface is observed, whereas the RS features a diffused interface. This discrepancy arises from the differing heat input and material flow patterns, with higher temperatures enhancing material plasticity and flow [49]. Consequently, base material in contact with the shoulder surface migrates effectively from the AS to the RS, contributing to the weld's overall structural integrity [50]. This detailed analysis underscores FSW's ability to overcome fusion welding limitations, producing superior welds with optimized material flow and thermal conditions.

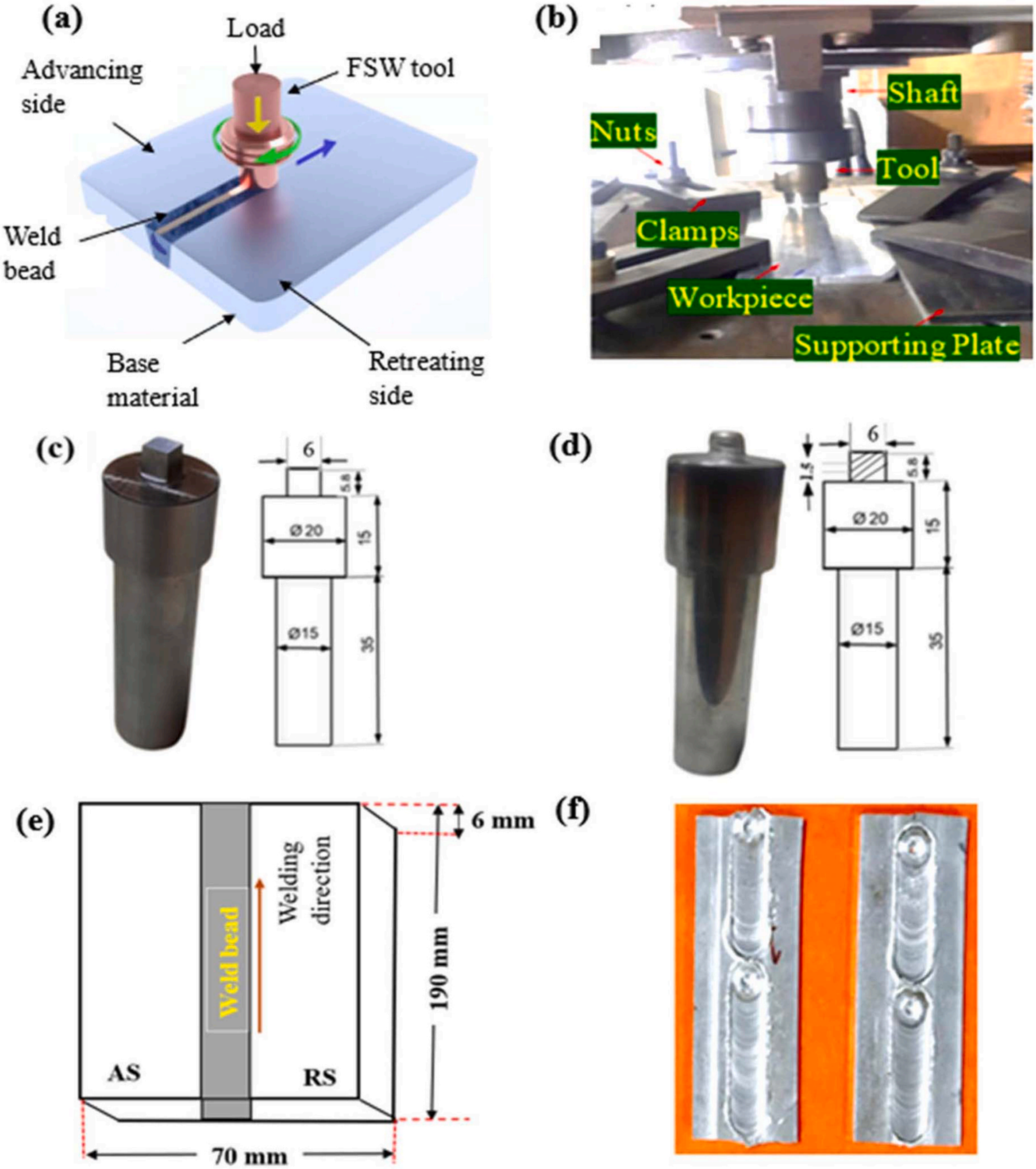

Fig. 2. (a) Schematic representation of FSW process, (b) FSW setup, (c) Square tool, (d) Circular threaded tool, (e) Butt joint design and (f) FSW weld plates (All dimensions are in mm).

Table 4
FSW tool specifications.

Particulars	Details
Tool shoulder diameter	20 mm
Tool pin length	5.8 mm
Tool pin profiles	Square (SQ) and circular threaded (CT)
Tool material	H13 tool steel

3.2. *Microstructure properties*

The cross-sectional analysis of the FSWed joint reveals significant microstructural changes across all the zones, highlighting the impact of thermal and mechanical processes during welding. These changes were quantitatively assessed using Image J software. In the BM, coarser grains dominate, with an average grain size (AGS) of 38 μm, as shown in Fig. 7(a). This coarse grain structure is characteristic of the base material, which has not undergone any plastic deformation or thermal cycling. In the TMAZ, the grains are elongated due to insufficient plastic deformation, as shown in Fig. 7(b). This elongation results from the combined effects of mechanical stirring and localized heat, which are not enough to fully recrystallize the material in this zone. The TMAZ is characterized by both mechanical deformation and heat exposure [51]. The temperature in the TMAZ is lower than in the NZ, leading to lower microhardness, with an AGS of 13 μm. In contrast, the NZ displays finer, recrystallized grains due to intense stirring and localized thermal conditions during the welding process, resulting in a reduced AGS in the NZ. The weld produced using the SQ tool pin profile achieved an AGS of 9

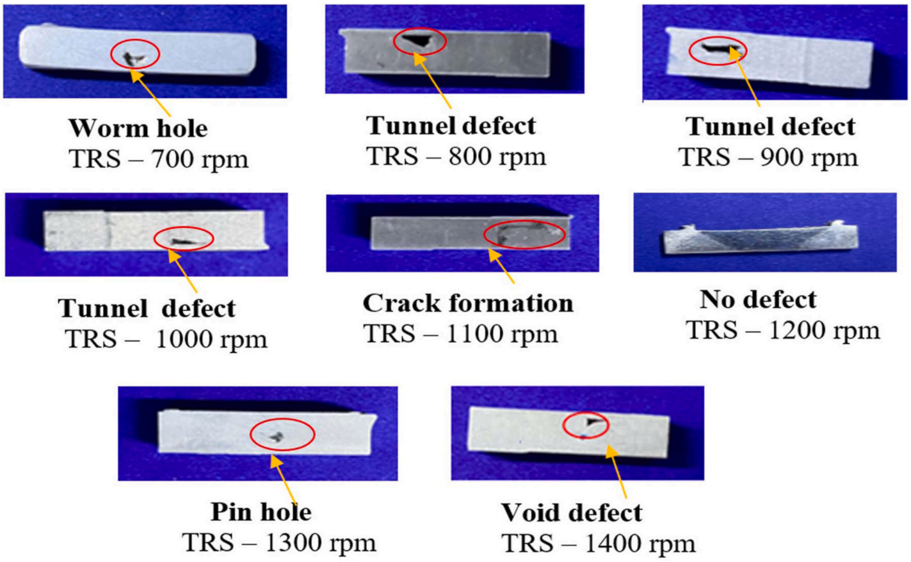

Fig. 3. Weld cross-sectional defects are observed during trial-and-error experiments.

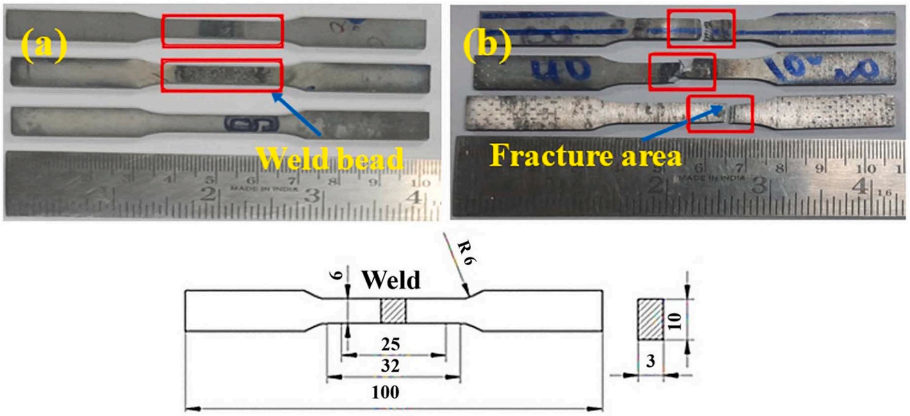

Fig. 4. Tensile test specimen (a) before test, and (b) after test (All dimensions are in mm).

μm in the NZ, as shown in Fig. 7(c). This fine-grain structure indicates dynamic recrystallization (DRX), which enhances the mechanical properties of the joint. Additionally, the HAZ exhibits larger grains compared to the TMAZ, as seen in Fig. 7(d). The grain coarsening in the HAZ is primarily due to exposure to elevated temperatures without sufficient mechanical stirring to refine the structure, with an AGS of 26 μm in this zone. This zone experiences thermal cycles that alter the microstructure but do not involve significant plastic deformation. Overall, observed microstructural variations across the zones coarser grains in the BM, elongated grains in the TMAZ, fine recrystallized grains in the NZ, and coarser grains in the HAZ underscore the complex interplay of heat and mechanical forces during FSW. These insights emphasize the importance of tool pin geometry, particularly the SQ profile, in achieving optimal grain refinement and joint quality.

The BM exhibits coarser grains, as shown in Fig. 8(a), which remain unaffected by the welding process. This coarseness indicates the absence of thermal or mechanical alteration in the BM, preserving its original grain structure. In the TMAZ, as depicted in Fig. 8(b), elongated grains are distinctly observed. This elongation is attributed to significant material flow and plastic deformation under the influence of mechanical stirring and localized heat. The deformation-induced strain in the TMAZ leads to some grain elongation, but the thermal energy is insufficient for full recrystallization, resulting in an AGS of 16 μm. In contrast, the NZ exhibits a refined microstructure with an AGS of 13 μm, as shown in Fig. 8(c). The noticeable grain size reduction in this zone is primarily a result of DRX, driven by the combined effects of intense plastic deformation and high strain rates during the stirring action of the tool. The effective strain rate within the NZ promotes the uniform redistribution of material, ensuring finer grains. Furthermore, the tool's shoulder diameter significantly impacts the heat input, which in turn affects the grain refinement process [52]. In the HAZ, as illustrated in Fig. 8(d), the grains are larger than those in the NZ and TMAZ, with an AGS of 29 μm. This can be attributed to the lower heat input in this region, which is insufficient to trigger DRX but enough to cause some grain growth. The thermal cycle in HAZ lacks the mechanical stirring necessary for grain refinement, resulting in coarser grains compared to plastically deformed zones. Overall, the observed microstructural variations across the zones emphasize the dynamic interplay between heat input, strain rate, and material flow during FSW. The finer grains in the NZ, elongated grains in TMAZ, and coarser grains in HAZ highlight the localized nature of the welding process and the critical influence of tool geometry and process parameters on microstructural evolution. Fig. 9 illustrates the average grain size across various weld regions for SQ and CT tools, including an error bar graph.

Using the SQ and CT tool pin profiles resulted in distinct microstructural characteristics across different cross-sectional levels, as shown in Figs. (10 and 11). The optical photomicrograph of the FSWed joint cross-section produced by the SQ tool pin is presented in Fig. 10,

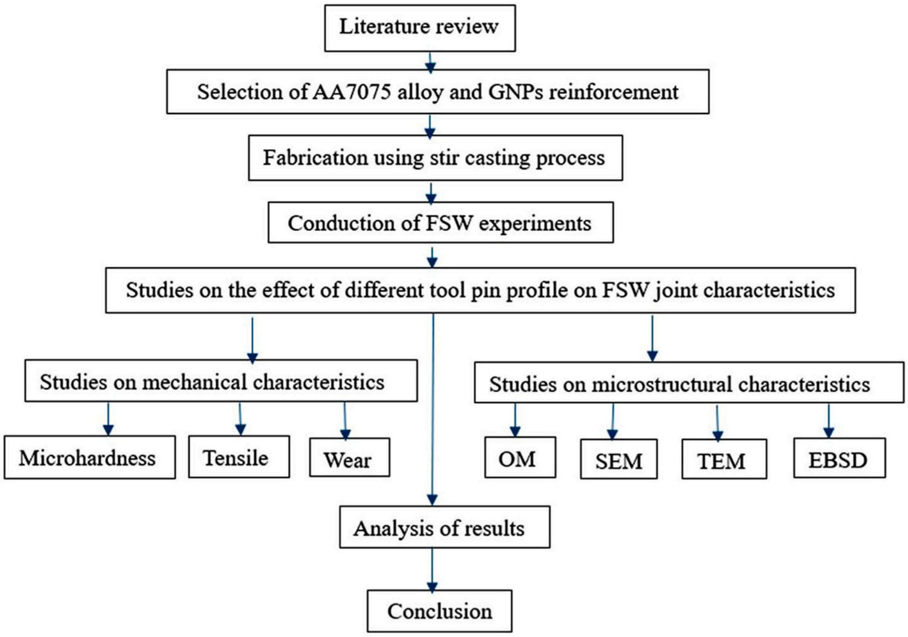

Fig. 5. Flow chart of research methodology.

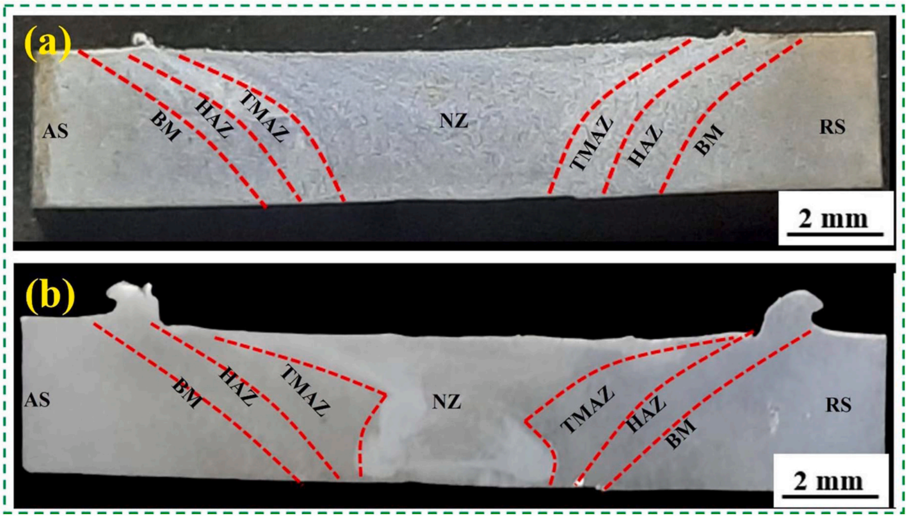

Fig. 6. Macroscopic observation of cross-sectional samples obtained by (a) SQ tool, and (b) CT tool.

highlighting variations in grain size and distribution across the weld thickness. At the upper weld surface, fine grains with an AGS of 9 μm are observed, as depicted in Fig. 10(a). These fine grains result from sufficient heat input at the top surface, facilitated by the direct contact of the shoulder tool. This localized heat input promotes DRX, leading to refined grains. At 1.5 mm below the surface, slightly coarser grains with an AGS of 12 μm appear, as shown in Fig. 10(b). This increase in grain size is attributed to the presence of non-homogeneous grains caused by variations in heat and material flow, leading to incomplete recrystallization. Further down, at 3 mm from the upper surface, the AGS increases to 16 μm, as shown in Fig. 10(c). This coarsening results from elongated grains formed due to lower heat input and the effects of a thermal cycle. The reduced heat and strain in this region are insufficient to facilitate uniform DRX, leading to larger, irregular grains. At 4.5 mm below the surface (Fig. 10(d)) and the lower weld surface (Fig. 10(e)), the grain structure becomes even coarser, with AGS values of 18 μm and 22 μm, respectively. This coarsening occurs primarily due to insufficient heat penetration into the lower weld regions [53].

The improper supply of heat in these areas limits the plastic deformation and recrystallization processes, resulting in larger, less refined grains. These findings demonstrate the critical influence of tool pin geometry and heat distribution on microstructural evolution across the weld cross-section. The SQ tool pin profile produces varying grain refinement levels, with finer grains near the upper surface due to higher heat and mechanical stirring, and progressively coarser grains towards the lower regions due to reduced heat input and deformation. These microstructural variations directly impact on the mechanical properties and performance of the FSWed joint.

The FSWed joint produced using the CT tool pin shows distinct microstructural variations across different cross-sectional levels, as illustrated in Fig. 11. These variations emphasize the impact of heat input and material flow on grain refinement throughout the weld thickness. At the upper surface, fine grains with an AGS of 11 μm are observed, as shown in Fig. 11(a). This fine-grain structure results from

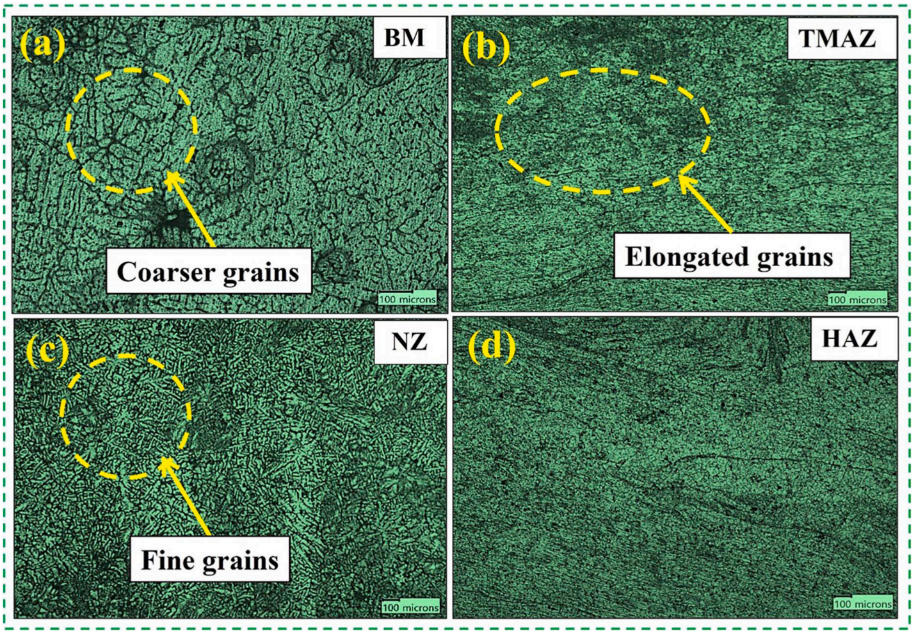

Fig. 7. Optical photomicrographs of SQ tool welds at (a) BM, (b) TMAZ, (c) NZ, and (d) HAZ.

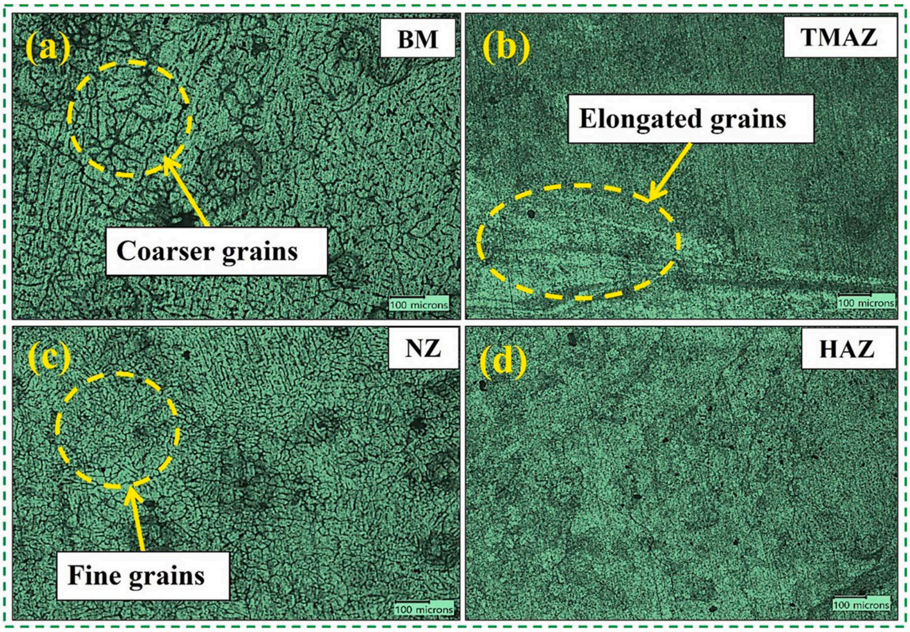

Fig. 8. Optical photomicrographs of CT tool welds at (a) BM, (b) TMAZ, (c) NZ, and (d) HAZ.

the high heat input generated by direct contact with the tool shoulder, combined with effective stirring action. DRX in this region facilitates refined and uniform grains due to optimal thermal and mechanical conditions [54,55]. At 1.5 mm below the surface, elongated grains with an AGS of 14 μm appear, as depicted in Fig. 11(b). These grains indicate reduced plastic deformation and moderate heat input, which are insufficient for complete DRX. As a result, the structure transitions between fine and coarse grains.

At 3 mm below the surface, coarser grains dominate, with an AGS of 18 μm, as represented in Fig. 11(c). This coarsening occurs due to inadequate heat input at this depth, limiting effective grain refinement. The reduced strain and thermal conditions contribute to the formation of irregular grains.

At a depth of 4.5 mm, the grains become more elongated, with an AGS of 21 μm, as shown in Fig. 11(d), reflecting further limitations in heat and stirring action. Finally, at the lower weld surface, a discontinuity in grain structure is observed, with an AGS of 24 μm, as depicted in Fig. 11(e). The lower region exhibits the largest grain sizes due to minimal heat input and inadequate plastic flow, which hinder recrystallization and lead to a coarse and irregular grain morphology.

These micrographs clearly demonstrate a gradual variation in grain size from the upper to the lower weld joint. The upper weld region achieves the finest grains due to higher heat input and consistent tool rotation, promoting uniform DRX. In contrast, the middle region exhibits moderately refined grains due to normal heat application, while the lower region features larger, less refined grains due to insufficient heat and mechanical stirring. This progressive grain size change across the weld thickness significantly impacts the joint's mechanical and

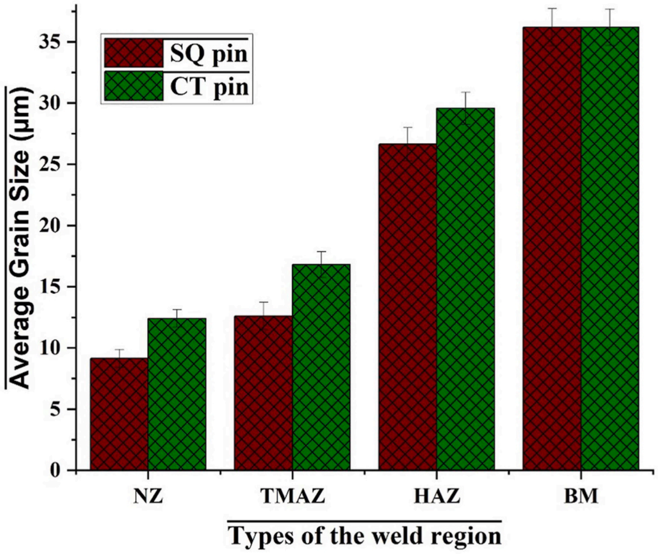

Fig. 9. Average grain size for different weld regions obtained by SQ and CT tools.

microstructural properties.

The SEM/energy dispersive spectroscopy (EDS) photomicrographs of FSWed joints produced using SQ and CT tool pins are detailed in Figs. (12 and 13), illustrating significant variations in microstructure and elemental composition. The use of SQ tool pin in the NZ resulted in fine grains with an AGS of 9 μm, as shown in Fig. 12(a). This refined structure is attributed to enhanced frictional contact between the tool shoulder and the workpiece, which generates sufficient heat and promotes effective DRX. Furthermore, the GNPs are homogeneously dispersed throughout the NZ, enhancing the material's uniformity and properties.

In the TMAZ, elongated grains are observed with an AGS of 13 μm, as shown in Fig. 12(b). The elongated grain structure reflects the interplay between plastic deformation and thermal gradients, indicating an intermediate zone of material flow and recrystallization. The HAZ exhibits a larger grain size, with an AGS 26 μm, as shown in Fig. 12(c). The absence of significant deformation in this region, coupled with lower heat input compared to NZ and TMAZ, results in coarser grains. The base material further reveals an AGS 38 μm, as seen in Figs. (12(d) and 13 (d)), indicating its original coarse-grained microstructure prior to welding.

The EDS analysis in the HAZ provides insights into elemental distribution, as shown in Fig. 12(e). The presence of aluminum (54.5 wt%), carbon (37.3 wt%), and zinc (4 wt%) confirms the elemental makeup and reflects the successful incorporation of GNPs within the weld. This analysis underscores the role of GNPs in enhancing the material properties of the welded joint. The FSW process relies heavily on the tool's design and function to achieve high-quality joints. The SQ tool pin enhances grain refinement and ensures consistent dispersion of GNPs due to its geometry, which improves material flow. The tool pin penetrates the base material during the FSW process, while the shoulder generates heat to soften the workpiece into a plastic state [53]. The tool pin agitates the softened material, enabling DRX and amalgamating the weld material. This mechanism is evident in the microstructural and compositional uniformity observed. It demonstrating the effectiveness of the SQ tool pin in achieving superior weld quality.

CT tool joints exhibit finer grains with an AGS of 13 μm, as shown in Fig. 13(a). This grain refinement in the NZ results from the DRX facilitated by the stirring action of the CT tool pin. However, the grains in the TMAZ are significantly elongated compared to those in the NZ, with an AGS of 16 μm, as illustrated in Fig. 13(b). The elongation is attributed to the reduced strain and less effective DRX in this transitional zone.

In the HAZ, the grain size enlarges further, attaining an AGS of 29 μm, as demonstrated in Fig. 13(c). The larger grain size in this region is due to the lower heat input and the absence of significant plastic deformation, which limits grain refinement. Point EDS analysis conducted on the HAZ area reveals a high carbon content (68.7 wt%), as shown in Fig. 13(e), indicating the dispersion of GNPs in this region.

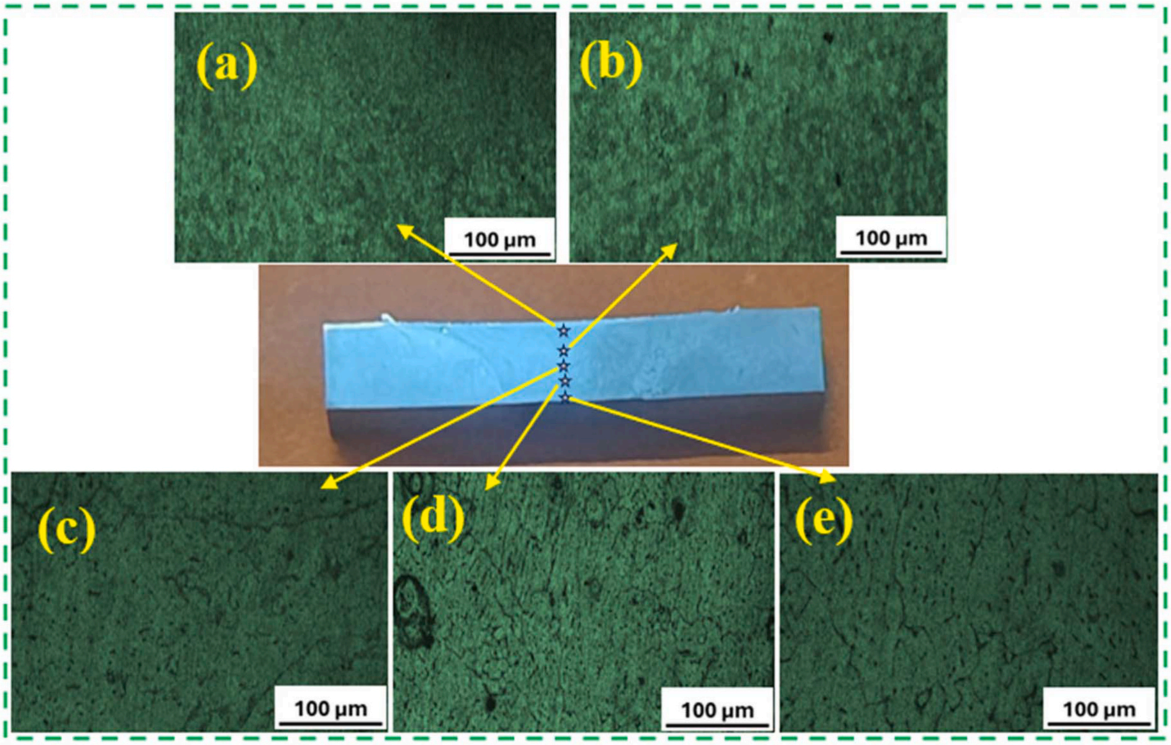

Fig. 10. Optical photomicrographs of SQ tool welds at (a) upper surface, and below the surface at (b) 1.5 mm, (c) 3 mm, (d) 4.5 mm, and (e) lower surface.

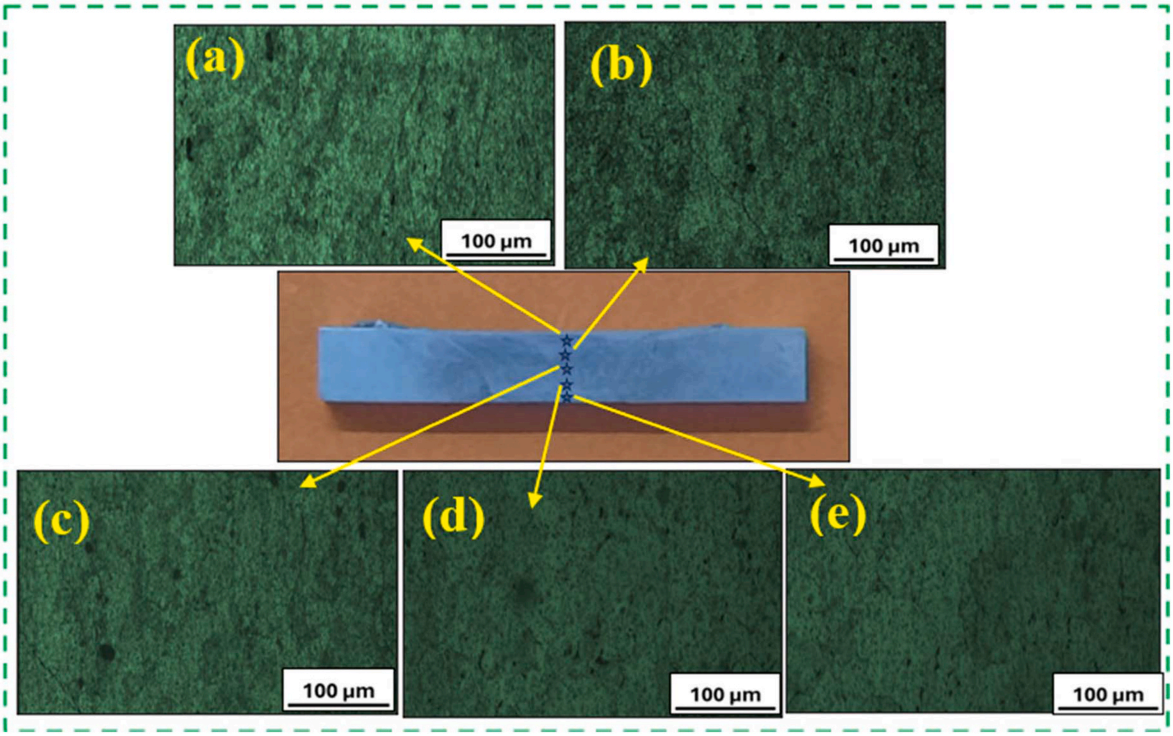

Fig. 11. Optical photomicrographs of CT tool welds at (a) upper surface, (b) 1.5 mm, (c) 3 mm, (d) 4.5 mm, and (e) lower surface.

Comparing the performance of the CT tool pin with the SQ tool pin reveals critical differences. The CT tool pin results in cracked grains and discontinuities in the microstructure across various weld regions. These defects contribute to lower tensile strength compared to the SQ tool pin. This difference arises from variations in material flow dynamics. The SQ tool effectively pushes the plasticized material downward while simultaneously directing it toward the tool pin center due to its flat face geometry. This dual action ensures better material mixing and a more uniform grain structure. The plasticized material flow is significantly influenced by the static-to-dynamic volume ratio, which determines how the material transitions from one side of the tool to the other. The rotating tool shoulder's interaction with the adjoining metal surfaces generates the frictional heat required for the material to reach a plastic state. The heat generation, in turn, is influenced by the coefficient of friction, which depends on the hardness of the tool. A higher coefficient of friction generally leads to increased heat input, which enhances material plasticity [55]. The SQ tool, with its flat faces, generates a pulsating action during the mixing process. This pulsation, occurring at a frequency of 4800 pulses/min at a rotational speed of 1000 rpm, improves the consistency of material mixing and contributes to superior weld quality [18,38]. The combination of higher heat input, efficient stirring action, and effective material flow makes the SQ tool pin superior for achieving defect-free and mechanically robust welds compared to the CT tool pin.

The SEM photomicrographs of the weld cross-section at 1.5 mm and 4.5 mm below the weld surface, obtained using SQ and CT tool pin profiles, are shown in Figs. (14 and 15). These images reveal distinct microstructural characteristics influenced by the tool pin geometry and the welding process parameters. In Fig. 14(a), representing the SQ tool pin at 1.5 mm below the surface, clear grain structures, grain boundaries, and the dispersion of GNPs reinforcements are evident. The consistent dispersion of GNPs in this region suggests effective DRX and adequate frictional heat generation during welding. However, Fig. 14(b), depicting the microstructure at 4.5 mm below the surface, reveals coarser grains. This coarsening is attributed to inadequate frictional contact between the tool pin and the workpiece, leading to insufficient heat input and suboptimal stirring in the lower regions. Similar trends are observed with the CT tool pin. Fig. 15(a), showing the microstructure at 1.5 mm below the surface, displays recrystallized grains but also highlights the presence of agglomerated GNPs. The uneven distribution of GNPs suggests a lack of consistent stirring, potentially caused by the limitations in the stirring action of the CT tool. This irregular distribution may negatively impact the mechanical properties of the weld. In Fig. 15(b), at 4.5 mm below the surface, the microstructure is characterized by larger grains. This grain enlargement results from reduced heat input and less effective plastic deformation in the lower weld region.

The comparison of SQ and CT tool pin profiles reveals that both produce larger grain structures in the lower weld region compared to the upper weld area. This variation is primarily due to the heat dissipation gradient along the weld thickness, which leads to less effective recrystallization and grain refinement in the lower regions. The SQ tool pin demonstrates relatively better grain refinement and GNPs dispersion in the upper weld area due to its superior frictional contact and stirring capabilities. In contrast, the CT tool pin exhibits limitations in maintaining uniform grain structure and reinforcement distribution, particularly in the lower weld regions. Overall, the results emphasize the importance of optimizing tool geometry, heat input, and stirring action to achieve consistent grain refinement and reinforcement dispersion across the weld cross-section, thereby enhancing joint performance and reliability. Additionally, similar results were observed, showing a significant improvement in strength and confirming that the GNPs bond effectively with the aluminum alloy [56].

The bright field TEM images of AA7075/GNPs joints fabricated using the square (SQ) tool are presented in Fig. 16. These images demonstrate significant grain refinement due to the addition of GNPs, which promote dynamic recrystallization, as well as the Zener–Hollomon effect. GNPs serve as heterogeneous nucleation sites for aluminum grains during solidification [57,58], as shown in Fig. 16(a). This enhances nucleation by accommodating the strain rate. A higher concentration of GNPs inhibits grain growth by acting as barriers, thereby reducing grain boundary mobility. As a result, GNPs strongly influence precipitation

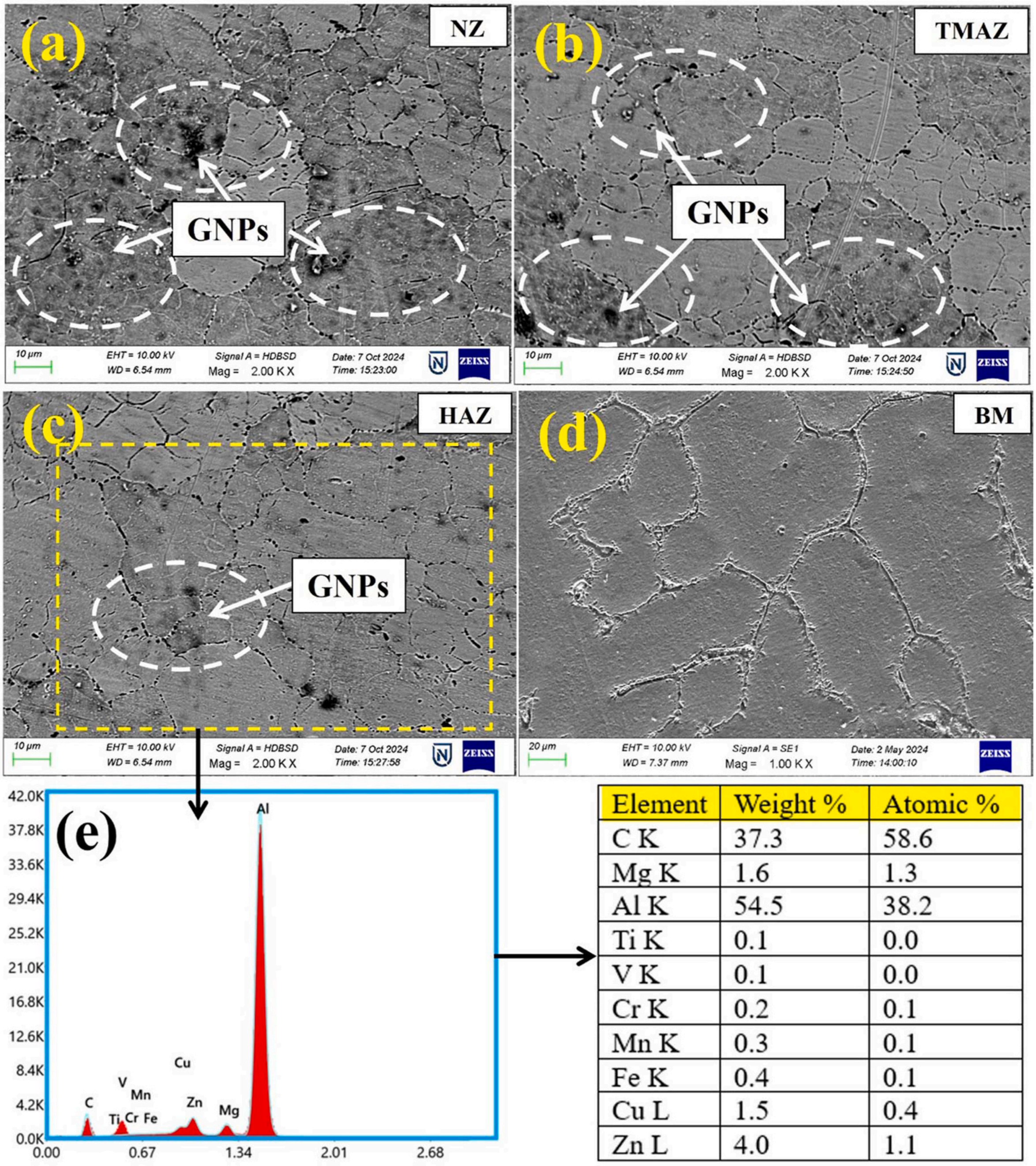

Element	Weight %	Atomic %
C K	37.3	58.6
Mg K	1.6	1.3
Al K	54.5	38.2
Ti K	0.1	0.0
V K	0.1	0.0
Cr K	0.2	0.1
Mn K	0.3	0.1
Fe K	0.4	0.1
Cu L	1.5	0.4
Zn L	4.0	1.1

Fig. 12. SEM photomicrographs obtained by SQ tool at (a) NZ, (b) TMAZ, (c) HAZ, (d) BM, and (e) EDS analysis.

behavior, leading to a fine-grained microstructure. Similar observations have been reported in the literature [59,60]. Additionally, the formation of η′ ($MgZn_2$) precipitates within the aluminum matrix, as shown in Fig. 16(b), plays a vital role in strengthening the weld. Fig. 16(c) illustrates the intercalation of aluminum and GNPs, where GNPs are uniformly dispersed throughout the aluminum matrix. The selected area electron diffraction (SAED) pattern in Fig. 16(d) corresponds to face-centered cubic (FCC) aluminum, with crystallographic planes (011) and (101) clearly identified.

Furthermore, Fig. 17 presents the TEM images of the AA7075/GNPs joint fabricated using the conical threaded (CT) tool. Fig. 17(a) shows the formation of precipitates within the nugget region. As illustrated in Fig. 17(b), GNPs are uniformly distributed throughout the nugget zone. The combined presence of these precipitates and uniformly dispersed GNPs contributes significantly to the overall weld strength. Fig. 17(c) reveals mechanical intercalation between aluminum and graphene. A strong interfacial bond between the GNPs and the AA7075 matrix is also observed, which is attributed to strain hardening caused by dislocation accumulation and effective stress transfer mechanisms. These phenomena enhance the material's strength during deformation [61,62]. The selected area electron diffraction (SAED) pattern, shown in Fig. 17(d), confirms the presence of a face-centered cubic (FCC) structure.

Moreover, the TEM image in Fig. 18(a) more distinctly illustrates the uniform distribution of precipitates within the weld region. As shown in Fig. 18(b), TEM analysis also indicates the development of sub-grains, attributed to dislocation movement and the recovery process. Additionally, these images clearly depict the interface between the GNP reinforcements and the aluminum alloy, demonstrating improved mixing in the weld area. Comparable observations regarding the bonding between GNP and aluminum have been reported by Khodabakhshi et al.

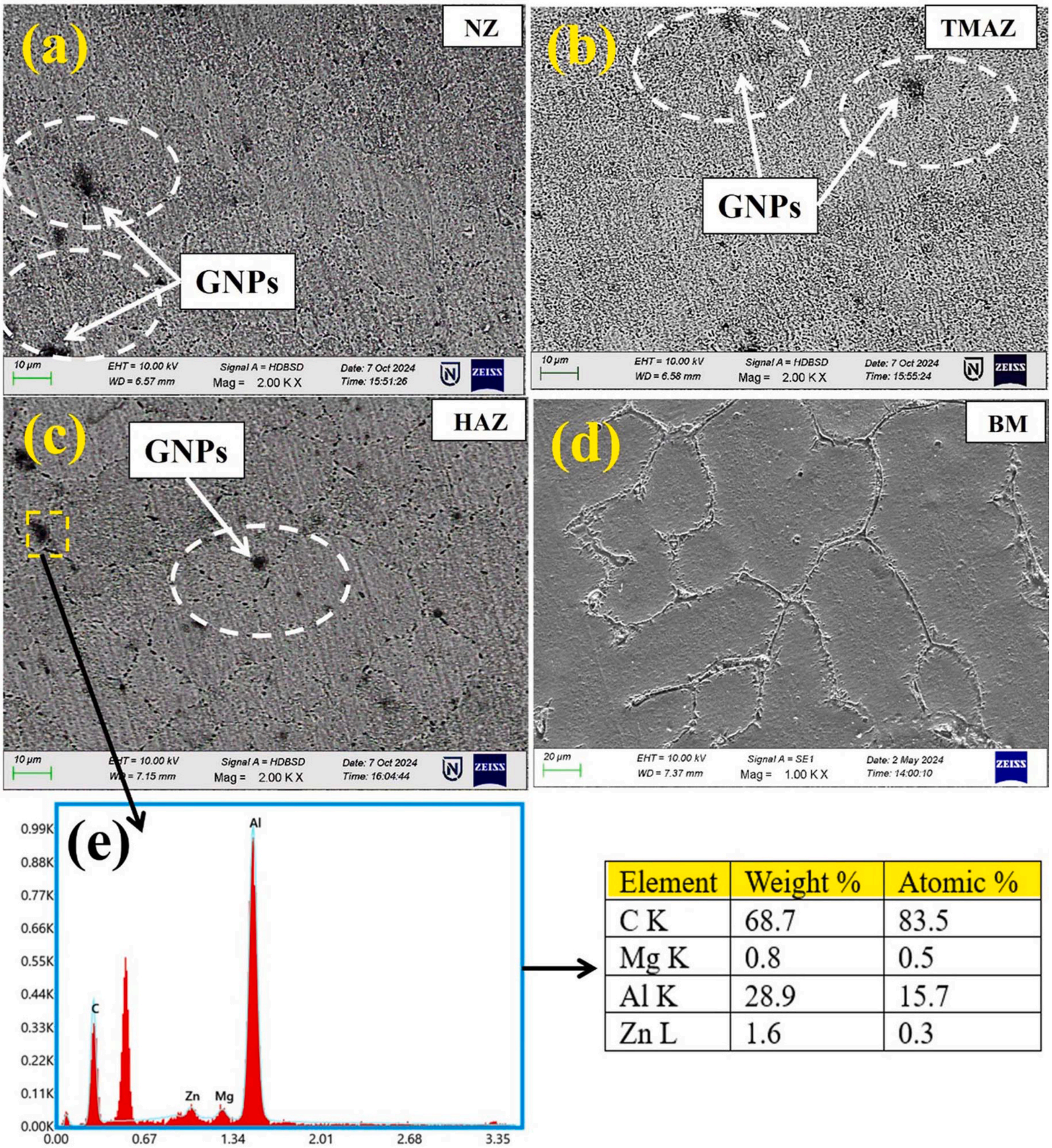

Element	Weight %	Atomic %
C K	68.7	83.5
Mg K	0.8	0.5
Al K	28.9	15.7
Zn L	1.6	0.3

Fig. 13. SEM photomicrographs obtained by CT tool at (a) NZ, (b) TMAZ, (c) HAZ, (d) BM, and (e) EDS analysis.

[63].

Furthermore, the average grain size (AGS) and misorientation angle (MA) for the SQ and CT tool joints were determined using EBSD analysis, as illustrated in Figs. 19 and 20, respectively. As shown in Fig. 19(a), the SQ tool produced a finer-grained microstructure compared to the coarser structure observed with the CT tool in Fig. 20(a). The formation of fine grains in SQ tool joints contributes to improved tensile strength and ductility. This is attributed to the SQ tool's rapid pulsating action and better plastic deformation coverage, facilitated by its four sharp edges, which promote more effective material flow than the CT tool.

Regardless of the tool used, the pinning effect of GNPs at grain boundaries is evident, as seen in Figs. 19(b) and 20(b). For SQ tool joints, an AGS of 10 μm and an average grain misorientation angle of 32.3° were observed, as depicted in Fig. 19(c) and (d). Similar results were reported by Shuai et al. [64]. In contrast, CT tool joints exhibited an AGS of 15 μm and an average misorientation angle of 34.3°. The presence of GNPs reduces dislocation density and acts as a barrier to plastic deformation in the AA7075 alloy, thereby enhancing both yield strength (YS) and ultimate tensile strength (UTS) [65]. The pole figures, shown in Figs. 19(e) and 20(e), represent crystal orientations, indicating how the crystallographic directions of aluminum alloy (001) and GNPs (0001) align relative to their respective axes. Each dot corresponds to the orientation of a single grain.

Fig. 21 shows the XRD patterns for GNPs, AA7075/GNPs composite, and FSWed AA7075/GNPs. The diffraction peak for GNPs at a 2θ angle of 26.5° corresponds to the (002) plane, indicating the presence of carbon. The AA7075/GNPs composite also confirms the presence of GNPs. In the FSWed AA7075/GNPs sample, the 2θ peak shifts slightly to 30°, with an additional peak near 36.5° corresponding to the (111) plane. Another peak appears at $2\theta = 44.6°$, associated with the (200) plane. The higher intensity peaks in the AA7075/GNPs composite are due to the high crystallinity of the material. During FSW, the heat input

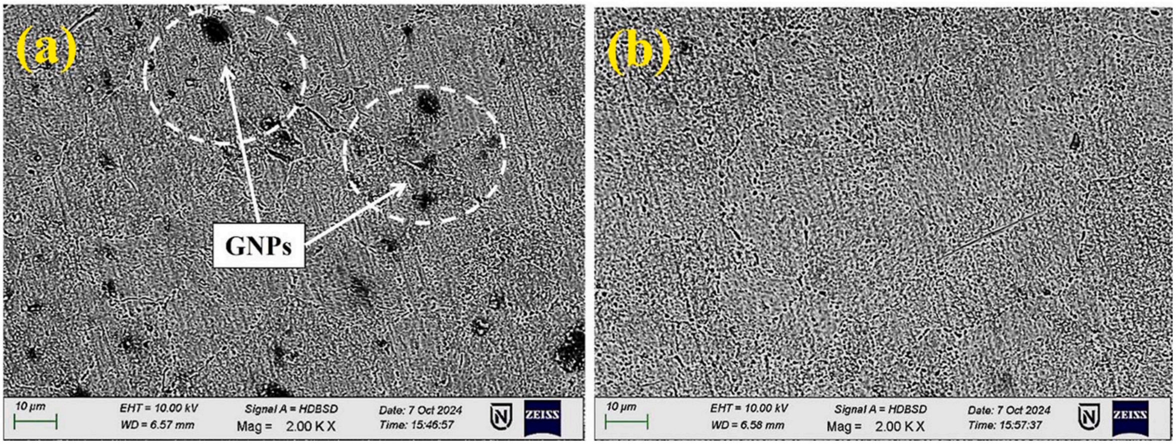

Fig. 14. SEM photomicrograph obtained by SQ tool pin at different level cross-sections below the weld surface (a) 1.5 mm, and (b) 4.5 mm.

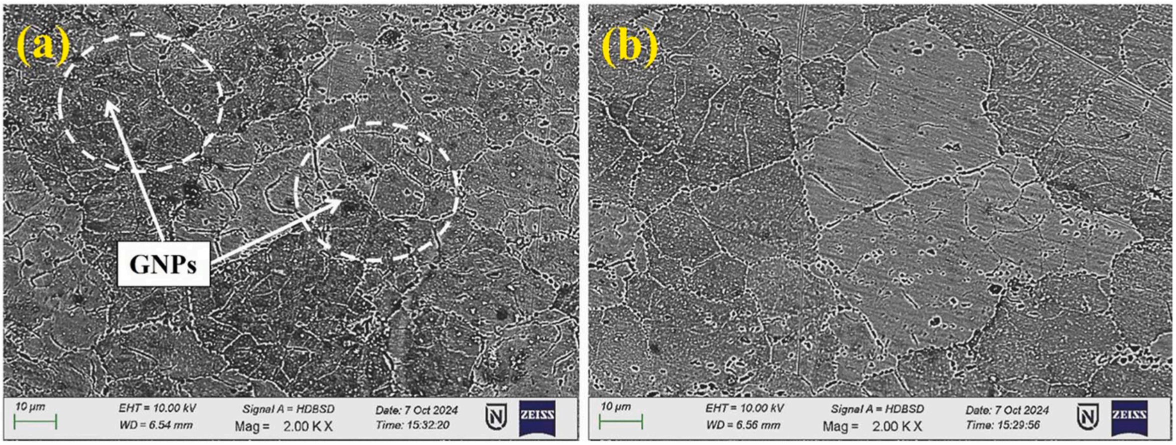

Fig. 15. SEM photomicrograph obtained by CT tool pin at different levels cross-section below the weld surface (a) 1.5 mm, and (b) 4.5 mm.

leads to greater deformation, causing strain between the base metal and the reinforcements. Typically, intermetallic compounds (IMCs) like Al_4C_3 form at the interface between aluminum and GNPs, enhancing ductility due to alloying between AA7075 and GNPs. Notably, no harmful needle-like IMC structures are detected in the XRD results, likely due to the controlled temperature conditions during FSW [66].

Additionally, the continuous dissolution of GNPs in the weld zone leads to the formation of IMCs such as Al_7Cu_2Fe, Mg_2Si, and $MgZn_2$. The intensity of these IMCs depends on the controlled presence of alloying elements. Peaks observed at 2θ values of 65.2°, 76.4°, and 78.3° correspond to the (220), (222), and (311) planes, respectively. These findings align with previous studies, where major peaks in aluminum matrix composites (AMCs) were noted at 38.3°, 44.6°, and 65.1° [2]. Some researchers have suggested that GNPs may not generate distinct carbon diffraction signals when processed via squeeze casting or pressure infiltration methods. However, in this study, due to the relatively low content of GNPs in the aluminum alloy, only small peaks were observed, indicating a lower but detectable dispersion in both the AA7075/GNPs composite and the FSWed sample.

Fig. 22 presents the Raman spectra of the AA7075 alloy, AA7075/GNPs composites, and FSWed AA7075/GNPs, which are used to assess the dispersion quality, bonding characteristics, and structural integrity of the weld joints. The Raman spectra of the composites prominently display three characteristic peaks: the D band, G band, and 2D band [67]. The D band is associated with structural defects and disorder in the crystal lattice, the G band reflects the graphitic nature of the material, and the 2D band provides information about the second-order Raman scattering, which relates to the stacking order of graphene layers. In the case of the AA7075 alloy, the Raman spectrum shows a G band peak at approximately 1536 cm^{-1} and a 2D band peak near 2800 cm^{-1}. For the AA7075/GNPs composite, peaks are observed at ~1360 cm^{-1} (D band), ~1532 cm^{-1} (G band), and ~2800 cm^{-1} (2D band). These peaks result from vibrational modes sensitive to the material's structural condition. The G band corresponds to the in-plane vibration of sp^2-hybridized carbon atoms, the D band indicates the presence of defects in the GNP lattice, and the 2D band reveals the number of graphene layers and their stacking configuration.

Uniform dispersion of GNPs in the aluminum matrix is critical for improving mechanical strength. Raman spectra help evaluate this distribution by analyzing the intensity of the D, G, and 2D bands across the samples. Additionally, the spectra provide insights into stress transfer from the AA7075 matrix to the GNPs. A lower intensity ratio ($I\_D/I\_G = 0.42$) in the AA7075/GNPs composite suggests a moderate level of structural defects, which may increase after processing due to chemical interactions between the matrix and reinforcements. The intensity ratio I_2D/I_G reflects the number of graphene layers. In the FSWed AA7075/GNPs sample, the G band shifts to ~1563 cm^{-1}, indicating stress in the GNPs, while the 2D band at ~2802 cm^{-1} shows signs of significant straining caused by the FSW process. The higher I_D/I_G ratio in the FSWed sample suggests smearing and damage to the GNPs under high stress, whereas the increase in I_2D/I_G indicates improved grain refinement and strengthening in the weld nugget [66,68].

As a general phenomenon, material deposition and loss from the tool surface are observed after the welding process due to the friction

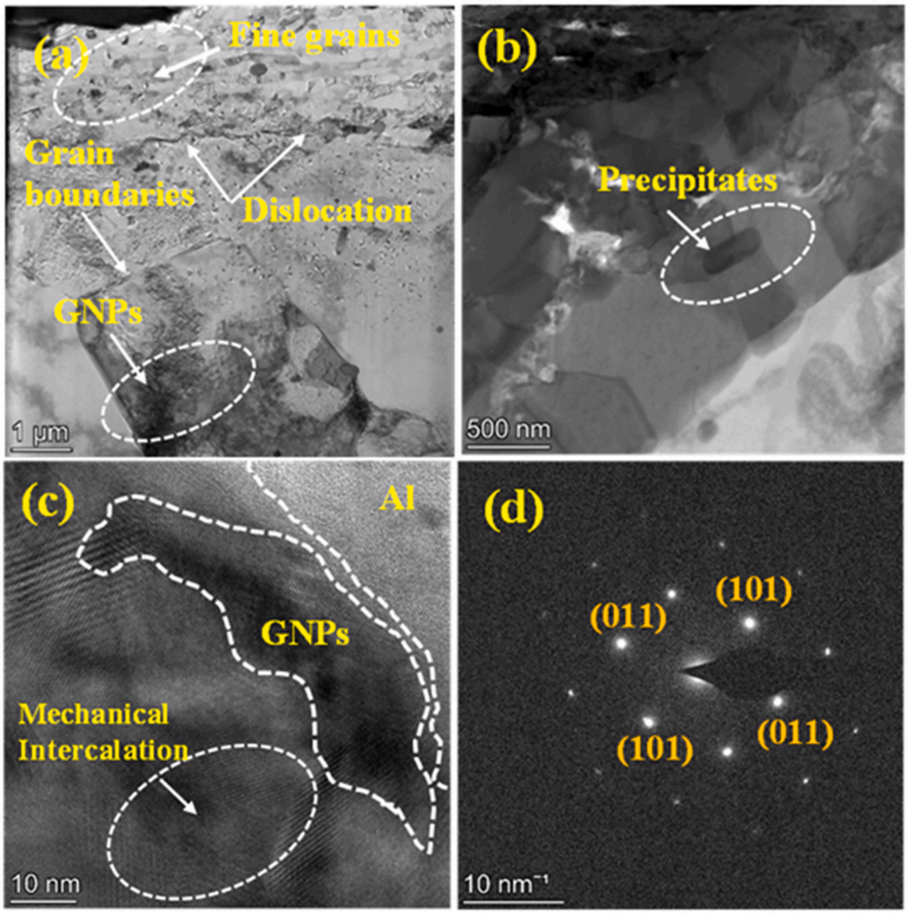

Fig. 16. Bright field TEM images of AA7075/GNPs joint obtained by SQ tool pin, (a) and (b) illustrate the presence of GNPs and precipitates, (c) Al-GNPs interface, and (d) SAED patterns for FCC grains.

between the tool and workpiece. This results in a noticeable change in the tool pin geometry, as shown in Fig. 23((a) and (b)) for the SQ and CT tools, respectively.

3.3. *Microhardness and tensile characteristics*

Vickers microhardness measurements were conducted along the cross-section of base material and FSWed joints to evaluate the hardness distribution and its relationship with the microstructural changes. Fig. 24(a) illustrates the microhardness profiles of AA7075, AA7075/GNPs, and weld joints produced using SQ and CT tools. The AA7075 alloy demonstrates an average microhardness 125 HV, while AA7075/GNPs exhibit a higher microhardness 135 HV, attributed to the reinforcement effect of GNPs. When the SQ tool pin is employed, the microhardness in NZ increases significantly, reaching 150 HV. This higher hardness is attributed to the finer grains and more uniform material flow facilitated by the SQ tool's enhanced frictional contact and stirring action. Similarly, the use of the CT tool pin results in a microhardness value of 141 HV in NZ. While this is lower than the SQ tool's value, it still indicates a substantial increase over the AA7075/GNPs hardness. The HAZ shows the lowest microhardness, mainly due to thermal softening in this region, where the material undergoes an unfavorable temperature effect during welding that reduces its hardness [69].

The formation of equiaxed grains in the NZ significantly contributes to the increased microhardness. This is because smaller, recrystallized grains hinder dislocation movement, thereby enhancing the material's strength [70]. Additionally, the grain refinement, which results in improved hardness values, aligns with the Hall-Petch relationship, which suggests that smaller grains enhance material strength. The Hall-Petch relationship is expressed in Eq. (1).

$$\int_y = \int_0 + k\, d^{-1/2} \qquad \text{(Eq. 1)}$$

Here, '$\int_y$' is yield strength, '$\int_0$' is the material's intrinsic strength, 'k' is a constant, and 'd' refers to the grain size diameter.

Compared to SQ/CT tool joints, AA7075/GNPs exhibit lower microhardness due to the presence of coarser grains, as shown in Figs.(7(a) and 8(a)), which further corroborates this relationship. The microhardness distribution across the joint highlights the influence of tool geometry and welding parameters on the final material properties, with fine grain structures resulting in improved hardness and, consequently, enhanced joint strength.

The tensile properties of AA7075, AA7075/GNPs, and FSWed joints fabricated using SQ and CT tool pins were thoroughly examined. The engineering stress-strain curve in Fig. 24(b) illustrates the significant influence of tool pin geometry on the tensile behavior of the weld joints. Key transverse tensile properties are YS, UTS, elongation (%), and joint efficiency (η)—were evaluated to determine mechanical performance. The stress-strain diagram was constructed using the mean values from three test readings.

AA7075 alloy exhibited YS 108 MPa, UTS 156.47 MPa, and elongation 1.6 %. Whereas, AA7075/GNPs showed improved mechanical properties, with YS 216 MPa, UTS 277 MPa, and elongation 2.1 %, attributed to the addition of GNPs and their effective bonding with the aluminum matrix. Among the welded joints, those produced with the SQ tool pin demonstrated superior tensile performance, achieving YS of 356 MPa, UTS of 630 MPa, and elongation of 6.9 %, along with a joint efficiency of 75 %, significantly surpassing the CT tool pin joints. The

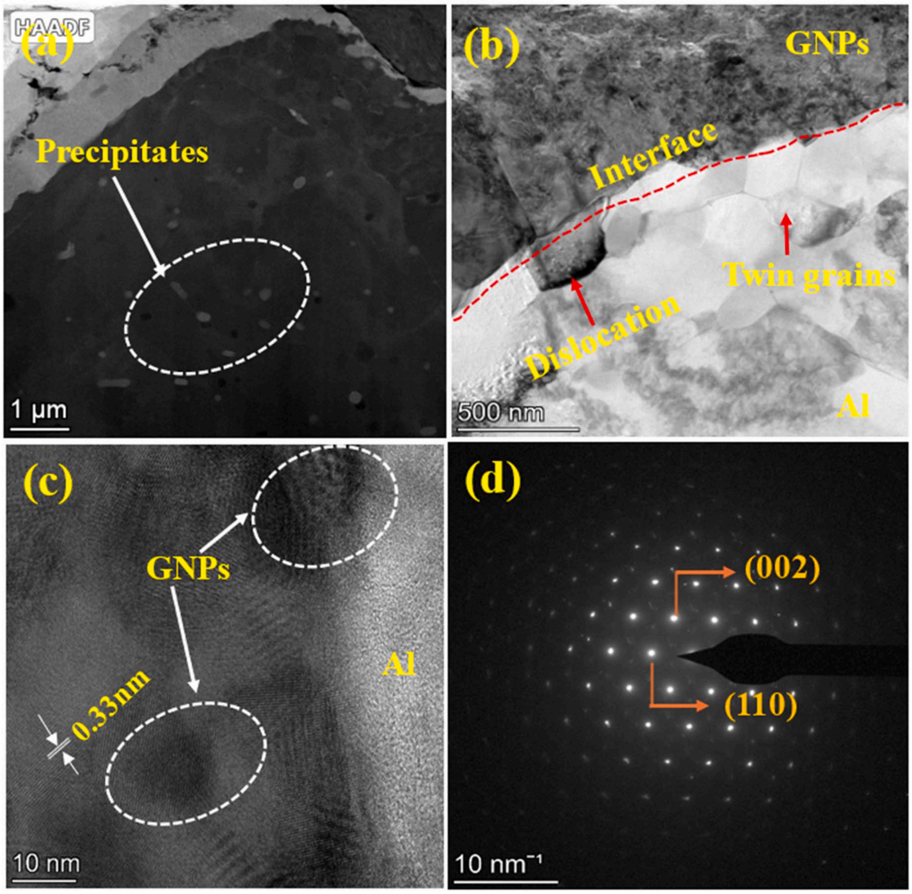

Fig. 17. Bright field TEM images of AA7075/GNPs joint obtained by CT tool pin, (a) and (b) illustrate the presence of precipitates and GNPs, (c) Al-GNPs interface, and (d) SAED patterns for FCC grains.

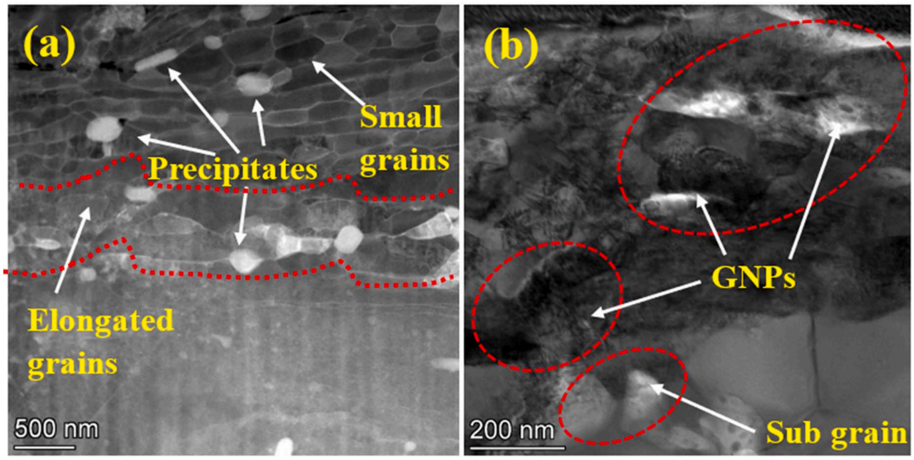

Fig. 18. TEM bright field images illustrate (a) precipitate dispersion, and (b) interface between aluminum alloy and GNPs.

error bar graph of UTS is presented in Fig. 24(c). This enhancement in tensile strength is primarily due to the fine and uniform grain structure formed during welding, as observed in Fig. 9. Additionally, the improved mechanical properties are associated with the formation of Guinier-Preston (GP) zones and η′ ternary (Al-Zn-Mg) precipitates, which contribute to weld strengthening.

Additionally, the SQ tool pin, with its four flat faces, generates a stronger pulsating material flow, further enhancing tensile strength by improving material distribution during welding. The SQ tool pin's ability to produce a well-bonded, recrystallized grain structure in aluminum alloy and disperse GNPs reinforcement significantly improves the weld's mechanical properties, supporting previous research on the benefits of grain refinement and uniform material distribution in enhancing tensile strength [26,35].

The FSW process significantly influences the distribution of microhardness across the weld joint, as illustrated in Fig. 25(a and b). The microhardness profile reveals a clear variation from the upper surface to deeper regions of the weld. At a depth of 1.5 mm below the upper weld surface, the microhardness achieved using the SQ tool is 148 HV, as shown in Fig. 25(a). However, this value is slightly lower than that

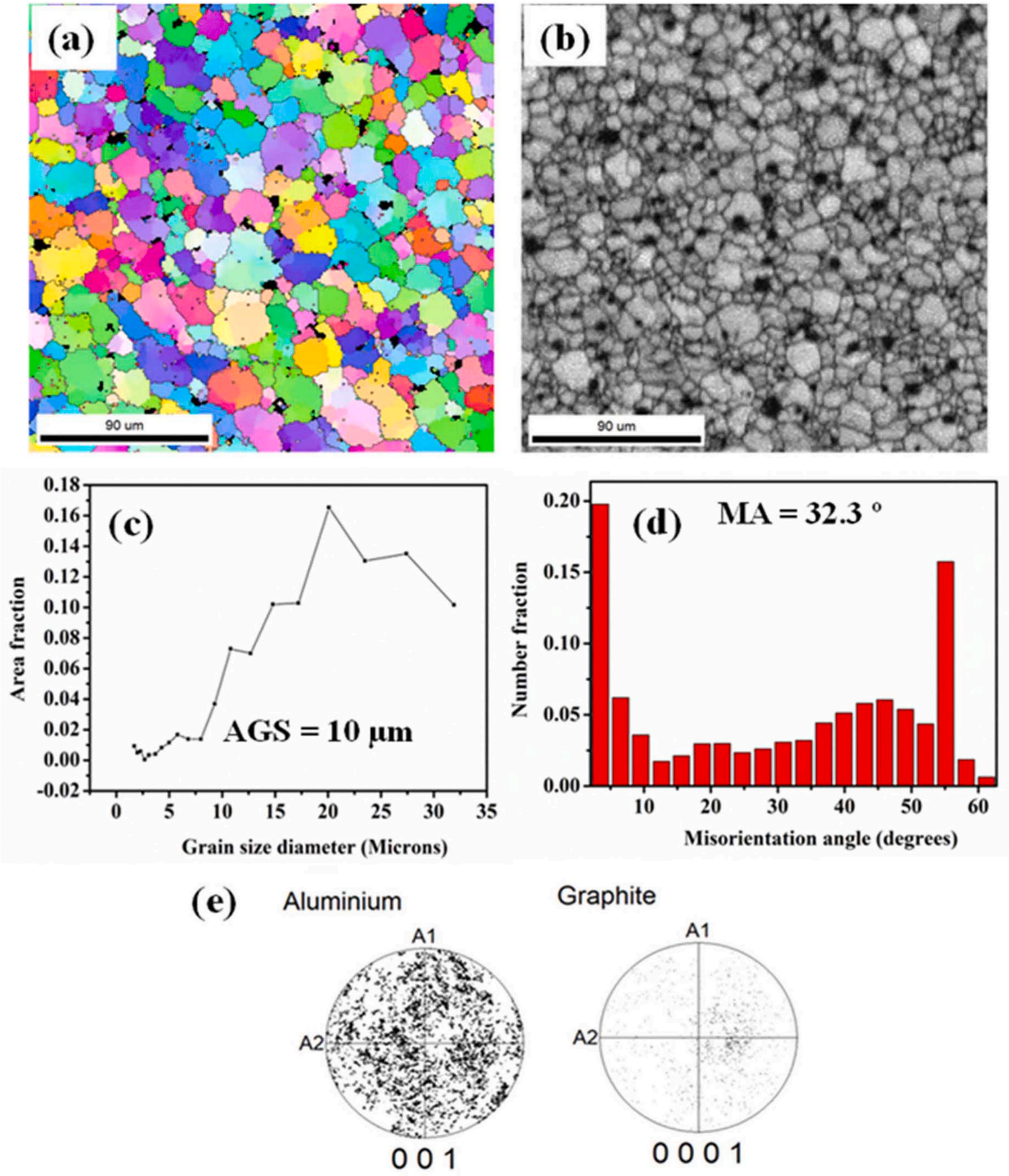

Fig. 19. EBSD image of FSW AA7075/GNPs joint obtained by SQ tool showing, (a) orientation map, (b) grain boundaries distribution, (c) average grain size (AGS), (d) misorientation angle (MA), and (e) pole figure.

observed at the top surface, which is attributed to a non-homogeneous dispersion of grains within this region. Despite this, the difference in microhardness between the AS and RS of the weld is minimal, indicating relatively uniform material properties across the joint.

As the depth increases, the microhardness gradually decreases. At 3 mm below the upper weld surface, the microhardness is reduced to 148 HV, as shown in Fig. 25(b). Similarly, at 4.5 mm depth, the microhardness drops further to 142 HV by the SQ tool pin, and at the lower surface of the weld, the microhardness reaches its lowest value of 128 HV by the CT tool pin. These results demonstrate that the lower weld region exhibits a lower microhardness compared to the upper surface. This can be attributed to the reduced heat input at the lower depth, which results in the formation of a coarser grain structure that does not benefit from the material softening seen at the upper surface.

Additionally, a comparison between the microhardness values obtained using the SQ and CT tool pins reveals a consistent trend. The average microhardness achieved with the CT tool pin is 10–15 HV lower than that produced by the SQ tool pin. This discrepancy is primarily due to the lower heat input generated by the CT tool, which does not induce as much material softening. In contrast, the SQ tool, with its flat shoulder, generates more heat, leading to a higher degree of material softening and, consequently, increased hardness in the weld zone. These microhardness findings are consistent with the observed microstructural differences, as shown in Figs. (14 and 15), further supporting the correlation between tool geometry, heat input, and the resulting material properties.

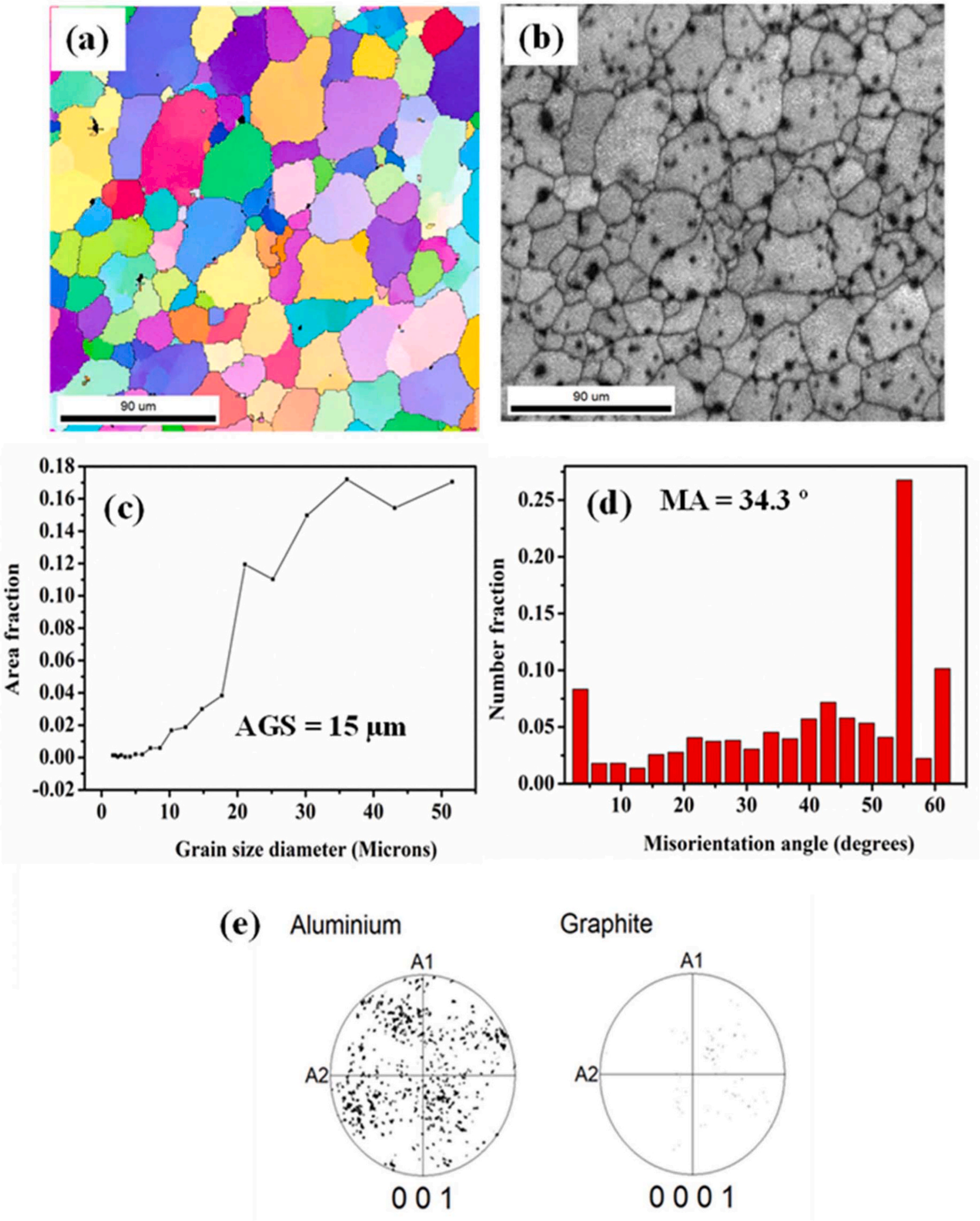

Fig. 20. EBSD image of FSW AA7075/GNPs joint obtained by CT tool showing, (a) orientation map, (b) grain boundaries distribution, (c) average grain size (AGS), (d) misorientation angle (MA), and (e) pole figure.

3.4. *Wear characteristics*

Wear analysis of AA7075, AA7075/GNPs and FSWed joints produced by SQ and CT tools was assessed for varying loads with a constant rotational speed of 300 rpm and a sliding velocity of 2.8 m/s, as illustrated in Fig. 26 ((a) and (b)). According to the Hall-Petch relationship, a decrease in grain size enhances material hardness, which directly influences wear resistance. When grain size is reduced, grain boundaries increase, acting as barriers to dislocation movement. This restriction in dislocation motion strengthens the material, reducing plastic deformation when subjected to frictional forces. As a result, material removal due to wear mechanisms is minimized, leading to improved durability. In contrast, materials with larger grain sizes have fewer boundaries, allowing dislocations to move more freely. This increased ease of deformation makes coarse-grained materials more susceptible to wear, resulting in higher wear rates. The wear rate was calculated using Eq. (2).

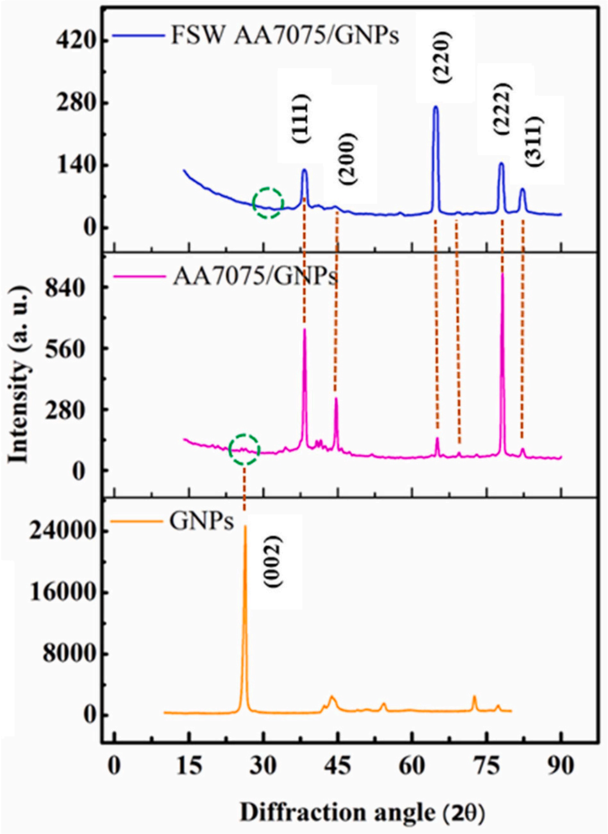

Fig. 21. XRD pattern of GNPs, AA7075/GNPs composites, and FSWed AA7075/GNPs.

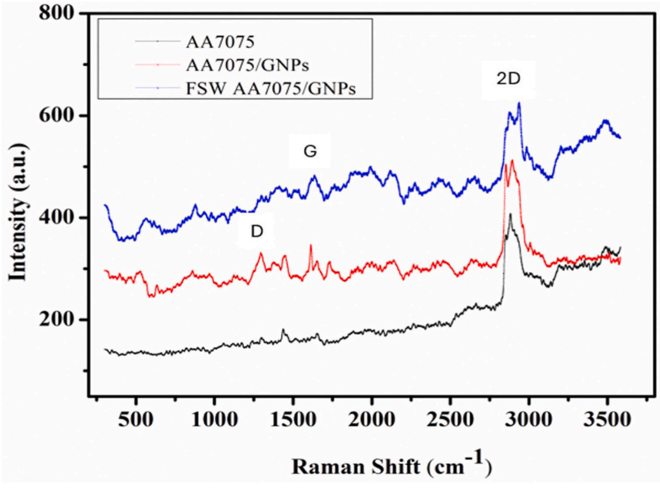

Fig. 22. Raman spectra of AA7075, AA7075/GNPs, and FSWed AA7075/GNPs.

$$\text{Wear rate} = \frac{V}{PL} \tag{Eq. 2}$$

where 'V' is the wear loss volume, 'P' is the load, and 'L' is the sliding distance.

The wear rate of AA7075 alloy decreases from 100 to 56 μm, while the wear rate for AA7075/GNPs reduces from 120 to 40 μm. The higher wear rate of AA7075 alloy compared to AA7075/GNPs is attributed to the presence of coarser grains with an AGS of 38 μm. In contrast, the CT tool joint, exhibiting an AGS of 13 μm, experiences a reduced wear rate from 80 to 48 μm. Furthermore, the SQ tool joint achieves the lowest wear rate, decreasing from 70 to 25 μm, due to its finer AGS of 9 μm. Regarding sliding distance, the wear rate of AA7075 alloy increases from 20 to 150 μm under a constant load of 20 N as the rotational speed rises from 100 to 400 rpm, which is attributed to the presence of coarser grains. According to the Hall-Petch relationship, wear resistance strength is influenced by grain size. The AA7075/GNPs composite exhibits a sliding distance ranging from 23 to 110 μm, while the SQ tool pin records the minimum sliding distance, varying from 31 to 80 μm. The coefficient of friction (CoF) for AA7075 alloy is found to be 0.8, as shown in Fig. 26(c), which is higher than that of SQ and CT tool joints. This reduction in CoF for SQ and CT joints is attributed to microstructural evolution and grain refinement in the weld zone, leading to improved strength and reduced friction. Similar wear behavior has been reported for FSW of AA7075 alloy [71,72].

Initially, wear rate is increased from 120 to 92 μm, as the load is increased from 30 to 40 N. During the early phase of wear, the wear debris acts as inhibitors to plastic deformation and adhesion, preventing further damage. After a certain sliding distance, the wear regime changes as the dislodged particles from the AA7075/GNPs integrate with the wear debris, which includes matrix material, worn particles, and iron (Fe) from the disc. These dislodged particles then fill the craters formed by the wear process, functioning as load-bearing elements within the wear debris and reducing the overall wear rate [73].

The wear rate under varying loads is dependent on the sliding distance, which can be calculated using Eq. (3).

$$\textit{Sliding distance} = \frac{\pi DNT}{60000} \tag{Eq. 3}$$

where 'D' is the diameter of the track in mm, 'N' is the speed of disc rotation in rpm, and 'T' is the time in seconds.

Fig. 27(a) illustrates the graph of frictional force versus load for AA7075, AA7075/GNPs, and CT/SQ tool joints under a load range of 10–40 N, with a constant disc rotational speed of 300 rpm. The frictional force of AA7075 increases from 3.39 N to 12.88 N, whereas AA7075/GNPs exhibits a lower frictional force ranging from 2.89 N to 10.78 N. This reduction in frictional force with GNPs is attributed to the solid lubrication effect, which leads to a decreased wear rate. Additionally, the SQ tool joint experiences a rise in frictional force from 2.23 N to 11.27 N, while the CT tool joint shows a higher range of 4.78 N–12.62 N. The lower frictional force in the SQ tool joint is due to its flat faces, which create intermittent contact with the workpiece, leading to reduced tool wear and improved material flow [72]. Similarly, as shown in Fig. 27(b), the frictional force of AA7075 increases from 4.2 N to 6.9 N, while AA7075/GNPs exhibits a range of 3.8 N–8 N. The SQ joint shows frictional forces between 4 N and 7.9 N, whereas the CT tool experiences a more significant increase, ranging from 3.7 N to 8.9 N.

This behavior could be attributed to the changes in the interaction between the rotating tool and the workpiece at higher speeds, where the frictional characteristics of the tool material and the workpiece interface play a more pronounced role in the frictional force generation. The increase in frictional force with higher speeds for the tool pin joints may also reflect differences in the material flow patterns and heat generation efficiency during the FSW process.

The worn surface of the samples was examined through SEM to assess the morphology, as shown in Fig. 28. The micrographs revealed that the wear mechanisms in all samples were primarily dominated by a combination of abrasion and adhesion. In the case of AA7075/GNPs, the wear debris appeared to be highly flaky and coarse in size, as depicted in Fig. 28(a). This is indicative of the relatively higher load of over 20 N, which facilitates the fracture and separation of material from the contact surfaces, leading to the formation of larger, more angular debris particles [74].

For the SQ tool pin, the wear debris exhibited a more diverse range of sizes and shapes, including small particles and elongated flakes, as shown in Fig. 28(b). This result suggests that the SQ tool pin promotes

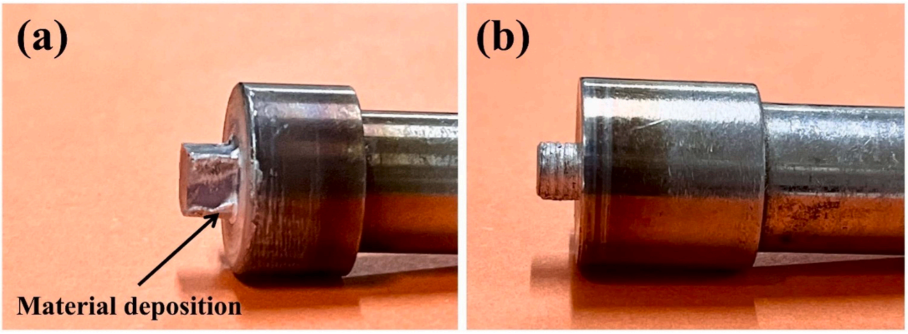

Fig. 23. Tool geometries after welding (a) SQ tool, and (b) CT tool.

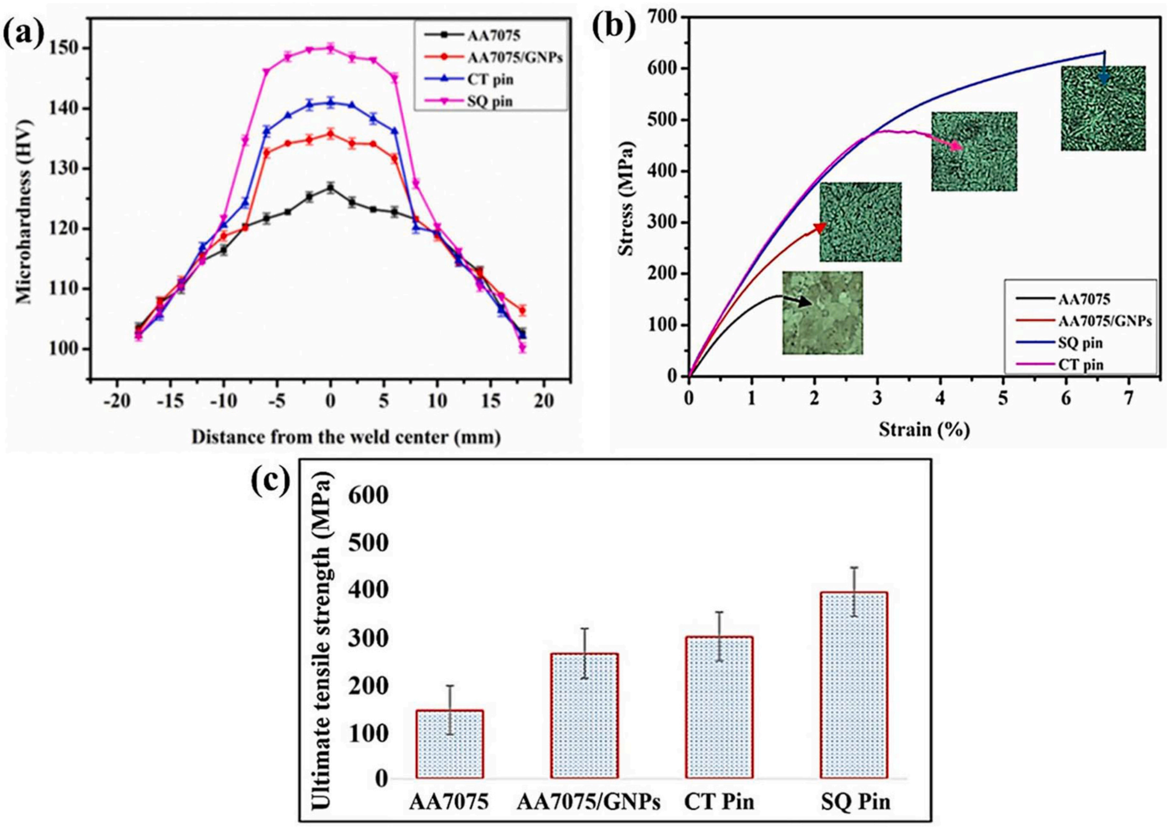

Fig. 24. (a) Microhardness profile for AA7075, AA7075/GNPs, CT and SQ joints (b) engineering stress–strain curve, and (c) error bar graph of ultimate tensile strength.

better material mixing during the welding process, which likely results in the more uniform distribution of wear debris. The better mixing leads to a finer and more evenly distributed debris morphology, reflecting lower friction and wear rates. In contrast, the CT tool pin resulted in wear debris consisting of more fragmented and crushed particles, including thin flakes of varying sizes, as shown in Fig. 28(c). This type of wear debris is typically associated with more severe wear and greater material deformation, which is a consequence of higher localized loads and stresses in this region. The lamellar structure of the wear debris further supports the observation that higher loads lead to greater material displacement and wear. As the wear debris size is smaller, it corresponds to a lower wear rate, confirming that the SQ tool pin, which produces finer debris, results in a lower overall wear rate compared to the CT tool pin.

3.5. *Fracture analysis*

The fracture surface of the weld joints, shown in Fig. 29(a–c), further corroborates these findings, revealing the nature of the material failure in both the joints. Fracture surface analysis was conducted on tensile test samples to assess the nature of the material failure. In the case of base material, i.e., AA7075/GNPs, the fracture surface displayed flat facets and ambiguous features, as seen in Fig. 29(a). These characteristics indicate limited plastic deformation, suggesting that the material exhibits brittle behavior under tensile stress. On the other hand, tensile test samples welded with the SQ tool pin exhibited a distinct fracture surface, showing uniform plastic deformation. As shown in Fig. 29(b), these samples displayed larger dimples, indicative of higher elongation in the joint. The presence of large intergranular cavities further reflects the extensive plastic flow in the material, which is a result of the SQ tool's ability to facilitate better bonding and fine-grain refinement. This

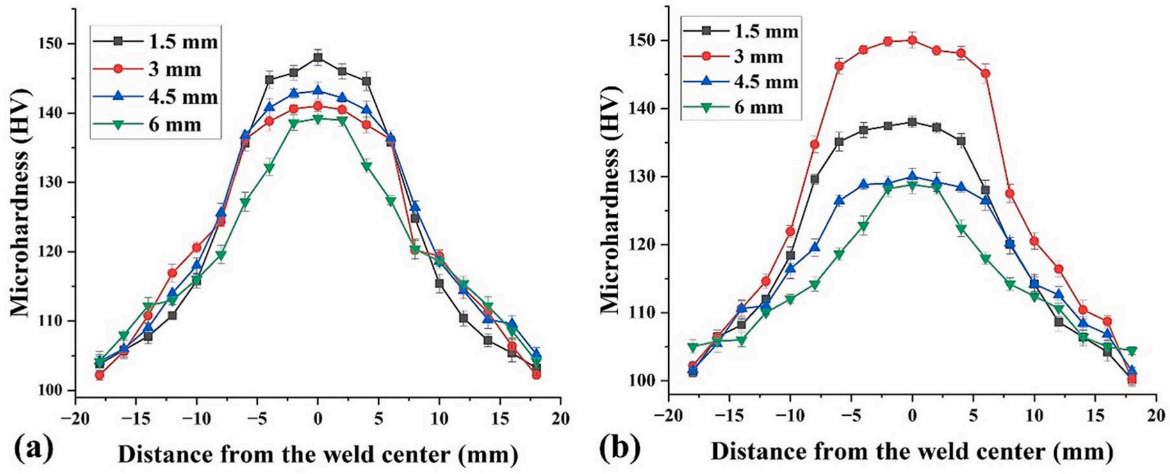

Fig. 25. Distribution of microhardness across the various levels of joint cross-section of welds obtained using (a) SQ tool pin, and (b) CT tool pin.

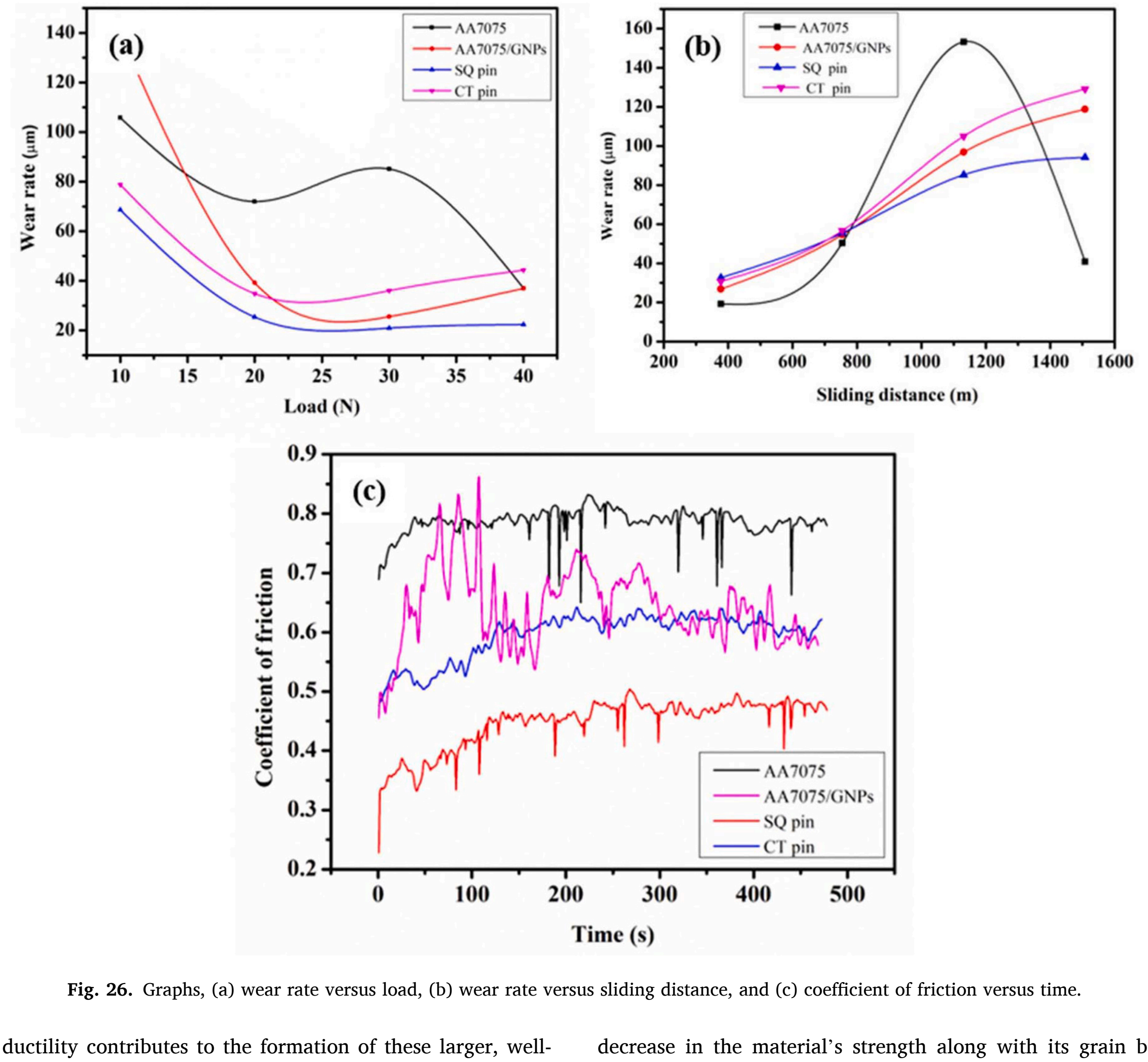

Fig. 26. Graphs, (a) wear rate versus load, (b) wear rate versus sliding distance, and (c) coefficient of friction versus time.

improved ductility contributes to the formation of these larger, well-defined dimples during fracture.

In contrast, the samples welded using the CT tool pin exhibited reduced hardness in the NZ and HAZ, which can be attributed to the dissolution of fine precipitates into the alloy and the presence of coarser grains in the HAZ region. The lack of precipitates in the HAZ leads to a decrease in the material's strength along with its grain boundaries, which in turn makes the material more susceptible to failure. The absence of fusion between the grains and the poor bonding between the alloy constituents in this region contribute to this weakness. As a result, failure is more likely to occur in the HAZ. The fracture surface from the CT tool pin, shown in Fig. 29(c), displayed relatively smaller dimples,

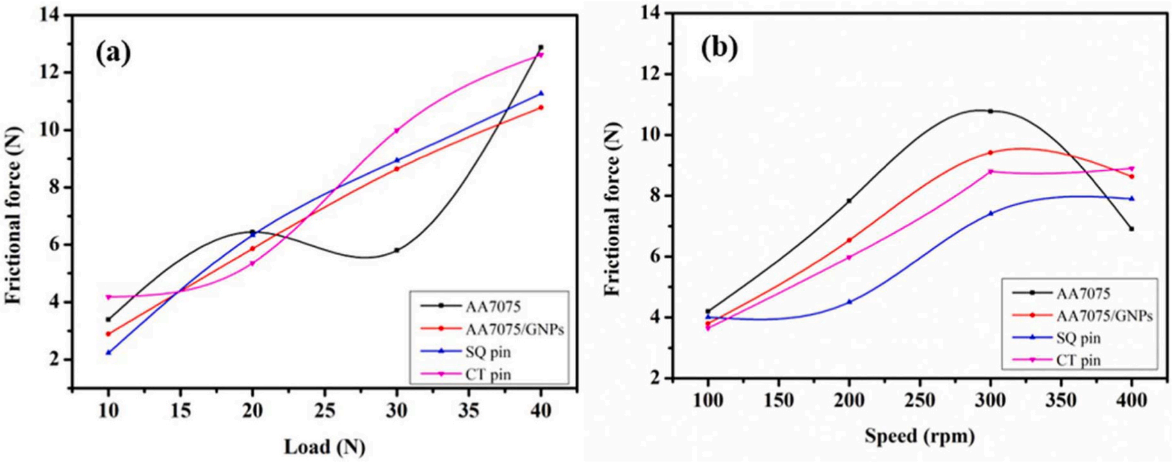

Fig. 27. Graphs, (a) frictional force versus load, and (b) frictional force versus speed.

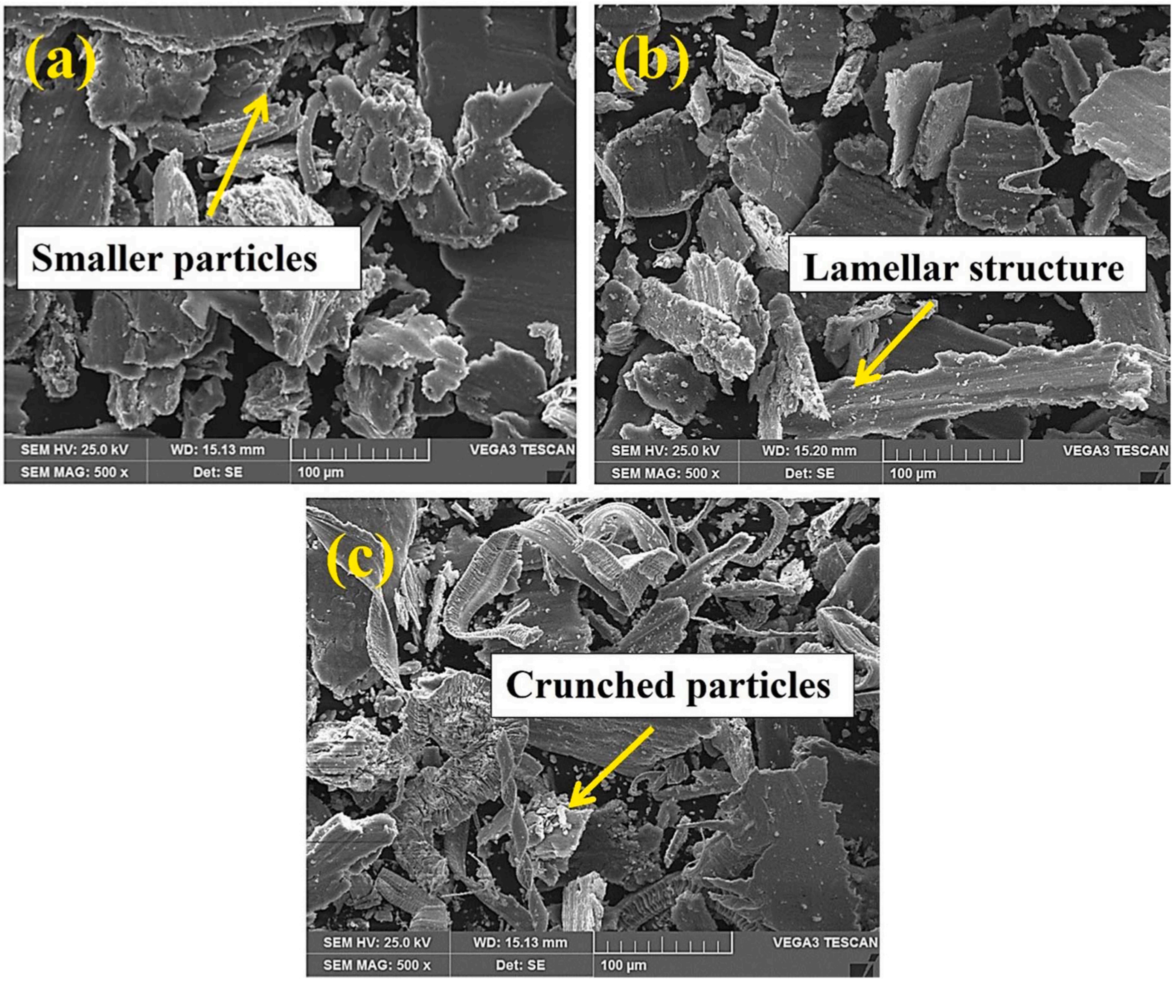

Fig. 28. Wear debris of (a) AA7075/GNPs, (b) SQ tool, and (c) CT tool.

which are indicative of insufficient plastic deformation. This is consistent with the reduced ductility observed in the CT tool welded joints. Similar studies have reported that joints produced using the CT tool pin exhibit lower joint efficiency compared to those produced by the SQ tool pin [75] supporting the conclusion that the SQ tool's superior heat generation and material flow result in enhanced tensile properties.

3.6. Limitations

In a study, various methodological limitations may arise, potentially influencing the conclusions. In this case, the methodology may have limitations due to differences in tool geometry, tool material, workpiece material, and the selection of process parameters. Additionally, the tool shape and material flow impact the efficiency of stirring and

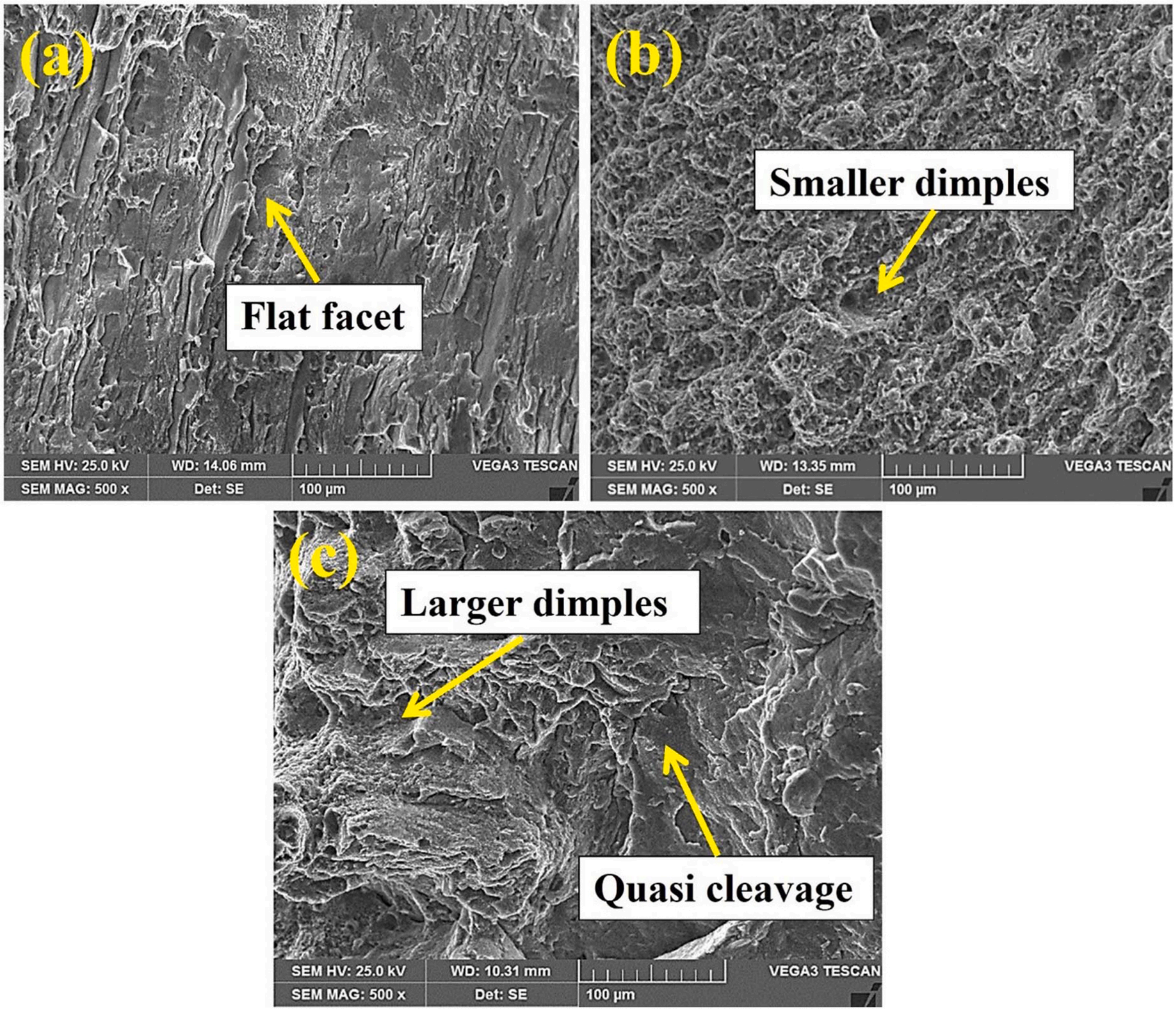

Fig. 29. SEM photomicrograph of fractured surface of (a) AA7075/GNPs, (b) SQ tool, and (c) CT tool joints.

consolidating the plasticized material. Tools may also lead to issues such as excessive flash, voids, or tunnel defects due to variations in material flow behavior. Furthermore, different tools generate varying amounts of heat, which can affect grain size, tensile strength, and hardness outcomes.

4. Conclusions

This research examines the impact of two distinct tool pin profiles on the weld characteristics of AA7075, focusing on microstructural changes and their influence on mechanical properties. The following results were derived from this study.

- The AA7075/GNPs, AMCs are fabricated successfully via stir casting technique. The GNPs are homogeneously dispersed at 1 wt% into aluminum matrix. Microstructure of stir cats samples reveal better bonding between the aluminum alloy and GNPs.
- In FSW process nugget zone (NZ) exhibits dynamic recrystallization, forming finer grains (10 μm for SQ, 15 μm for CT), which improve material uniformity and contribute to enhanced strength and durability in the welded joint.
- In the thermo-mechanically affected zone (TMAZ), elongated grains (14 μm for SQ, 18 μm for CT) are formed due to thermal cycling and plastic deformation, impacting the overall microstructure but not achieving full recrystallization.
- The heat-affected zone (HAZ) exhibits coarser grains (up to 29 μm), primarily due to lower stirring and reduced heat input, leading to less refined material properties compared to the nugget and thermo-mechanically affected zones.
- Joints fabricated using the SQ tool pin demonstrated superior mechanical performance, achieving a higher microhardness of 150 HV and tensile strength of 630 MPa, in contrast to the CT tool, which recorded 141 HV and 478 MPa. This represents a 75 % enhancement in joint efficiency.
- The wear rate of the AA7075 alloy decreased from 100 μm to 56 μm, while the AA7075/GNPs composite showed a reduction from 120 μm to 40 μm. The comparatively higher wear rate in the AA7075 alloy is linked to its coarser grain structure, with an average grain size (AGS) of 38 μm. In contrast, the SQ tool joint exhibited the lowest wear rate, dropping from 70 μm to 25 μm, attributed to its refined microstructure with an AGS of 10 μm.
- The frictional force for the AA7075 alloy increased from 4.2 N to 6.9 N, while the AA7075/GNPs composite exhibited a range between 3.8 N and 8.0 N. The SQ tool joint experienced frictional forces between 4.0 N and 7.9 N, whereas the CT tool joint showed a more pronounced increase, ranging from 3.7 N to 8.9 N.

Nomenclature/Abbreviation

AS	Advancing side
AMCs	Aluminum matrix composites
AGS	Average grain size
BM	Base material
CT	Cylindrical threaded
CNTs	Carbon nanotubes
CoF	Coefficient of friction
DRX	Dynamic recrystallization
EDS	Energy dispersive spectroscopy
FCC	Face centered cubic
FSW	Friction stir welding
FSWed	Friction stir welded
FSP	Friction stir processing
GP	Guinier-Preston
GNPs	Graphene nanoplatelets
HV	Vickers hardness
HAZ	Heat-affected zone
MWCNT	Multiwall carbon nanotube
MIG	Metal inert gas
NZ	Nugget zone
OM	Optical microscopy
PSN	Particle stimulated nucleation
PCA	Pin cone angles
RS	Retreating side
SQ	Square
SEM	Scanning electron microscopy
TMAZ	Thermo-mechanically affected zone
TIG	Tungsten inert gas
TRS	Tool rotational speed
TTS	Tool traverse speed
UTS	Ultimate tensile strength
YS	Yield strength
σ_y	Yield strength
σ_0	Intrinsic strength
k	Constant
d	Grain size diameter
D	Diameter of the track
%	Elongation
η	Joint efficiency
V	Wear loss volume
P	Load
L	Sliding distance
N	Speed of disc rotation
T	Time

Data availability statement

The datasets generated and analyzed during the current study are available from the corresponding author on reasonable request.

Authors contributions

All authors have read and approved the final version of the manuscript. The author's contributions are as follows: Rahul Biradar: Conceptualization, Methodology, Investigation, Writing—draft Manuscript; Sachinkumar Patil: Resources, Supervision, Validation, Writing – review & editing; Nagamadhu M: Visualization, Data Curation, Formal Analysis; Priyaranjan Sharma & Filipe Fernandes: Project Administration, Funding Acquisition, Writing – review & editing.

Funding declaration

Sachinkumar Patil thanks REVA University, India Bengaluru for the continuous support of funding and for providing the facility to carry out the research [Ref No. RU. EST. ME: 2022-1]. Filipe Fernandes acknowledges the national funds through FCT – Fundação para a Ciência e a Tecnologia, Portugal under projects UID/00285 - Centre for Mechanical Engineering, Materials and Processes and LA/P/0112/2020.

Declaration of interest

The authors declare that they have no competing financial or non-financial interests that could influence the research findings presented in this manuscript. This statement ensures transparency and upholds ethical publishing standards.

References

[1] Hamdollahzadeh A, Bahrami M, Farahmand NM, Yusefi A, Besharati MK, Parvin N. Microstructure evolutions and mechanical properties of nano-SiC-fortified AA7075 friction stir weldment: the role of second pass processing. J Manuf Process 2015;20(1):367–73. https://doi.org/10.1016/j.jmapro.2015.06.017.

[2] Sunil R, Tanmoy D, Ajay MS, Jinu P. Fabrication and characterization of Al/GNPs composite by bottom pouring stir casting. Mater Lett 2022;327:133002. https://doi.org/10.1016/j.matlet.2022.133002.

[3] Liwen C, Yuhong Z, Muxi L, Limin L, Hou Lifeng. Reinforced AZ91D magnesium alloy with thixomolding process facilitated dispersion of graphene nanoplatelets and enhanced interfacial interactions. Mater Sci Eng A 2021;804:140793. https://doi.org/10.1016/j.msea.2021.140793.

[4] Mahmood K, Rafi WH, Muhammad AB, Shahid A, Abdul W, Ragnhild EA. Study of microstructure and mechanical behaviour of aluminium alloy hybrid composite with boron carbide and graphene nanoplatelets. Mater Chem Phys 2021;271:124936. https://doi.org/10.1016/j.matchemphys.2021.124936.

[5] Stankovich S, Dikin DA, Dommett GHB, Kohlhass KM, Zimney EJ, Stach EA. Graphene-based composite materials. Nature 2006;442:282–6. https://doi.org/10.1038/nature04969.

[6] Jian L, Haixue Y, Kyle J. Mechanical properties of graphene platelet-reinforced alumina ceramic composites. Ceram Int 2013;39(6):6215–21. https://doi.org/10.1016/j.ceramint.2013.01.041.

[7] Shin SE, Bae DH. Deformation behavior of aluminum alloy matrix composites reinforced with few-layer graphene. Composites Part A 2015;78:42–7. https://doi.org/10.1016/j.compositesa.2015.08.001.

[8] Omid G, Mehran Z, Behzad N, Benjamin C Church, Pradeep KR. Selected challenges in solidification processing of graphene nanoplatelets (GNPs) reinforced aluminum alloys composites. Front Mater 2024;11. https://doi.org/10.3389/fmats.2024.1363270.

[9] Li JL, Xiong YC, Wang XD, Yan SJ, Yang C, He WW. Microstructure and tensile properties of bulk nanostructured aluminum/graphene composites prepared via cryomilling. Mater Sci Eng A 2015;626:400–5. https://doi.org/10.1016/j.msea.2014.12.102.

[10] Wenzheng Z, Xiaoliang S, Jie Y, Ahmed I, Zengshi X, Qingshuai Z, et al. Investigation of mechanical and tribological behaviors of multilayer graphene reinforced Ni3Al matrix composites. Compos. Part B Eng 2015;70:149–55. https://doi.org/10.1016/j.compositesb.2014.10.052.

[11] Deore HA, Bhardwaj A, Rao AG, Mishra J, Hiwarkar VD. Consequence of reinforced SiC particles and post process artificial ageing on microstructure and mechanical properties of friction stir processed AA7075. Def Technol 2019;16(5):1039–50. https://doi.org/10.1016/j.dt.2019.12.001.

[12] Xiangbin W, Diana A. Friction stir welding of similar aluminum alloys thick plates: understanding the material flow, microstructure evolution, defect formation, and mechanical properties. Materialia 2022;24:101508. https://doi.org/10.1016/j.mtla.2022.101508.

[13] Ahmed MMZ, Sabbah A, Seleman MMS, Ammar HR, Ahmed E. Friction stir welding of similar and dissimilar AA7075 and AA5083. J Mater Process Technol 2017;242:77–91. https://doi.org/10.1016/j.jmatprotec.2016.11.024.

[14] Praveen R, Koteswara SR, Selvakumar G, Damodaram R. High-Velocity Projectile Impact behaviour of friction stir welded AA7075 thick plates. Def Technol 2023;29:153–63. https://doi.org/10.1016/j.dt.2023.01.019.

[15] Heidarzadeh S, Mironov R, Kaibyshev G, Çam A, Simar A, Gerlich F, Khodabakhshi A, Field DP, Robson JD, Deschamps A, Withers PJ. Friction stir welding/processing of metals and alloys: a comprehensive review on microstructural evolution. Prog Mater Sci 2021;17:100752. https://doi.org/10.1016/j.pmatsci.2020.100752.

[16] Yu C, Zhihui C, Hua D, Fenghe Z. The evolution of the nugget zone for dissimilar AA6061/AA7075 joints fabricated via multiple-pass friction stir welding. Metals 2021;11:1506. https://doi.org/10.3390/met11101506.

[17] Feng AH, Chen DL, Zy MA. Microstructure and cyclic deformation behavior of a friction-stir-welded 7075 Al Alloy. Metall Mater Trans 2010;41:957–71. https://doi.org/10.1007/s11661-009-0152-3.

[18] Bahrami M, Besharati MK, Dehghani K, Parvin N. On the role of pin geometry in microstructure and mechanical properties of AA7075/SiC nano-composite fabricated by friction stir welding technique. Mater Des 2014;53:519–27. https://doi.org/10.1016/j.matdes.2013.07.049.

[19] Joshi A, Gope A, Gope PC. Effect of post-weld heat treatment on mechanical properties and fatigue crack growth behaviour of friction stir welded 7075-T651 Al alloy. Theor Appl Fract Mech 2023;123:103714. https://doi.org/10.1016/j.tafmec.2022.103714.

[20] Chaitanya S, Dheerendra D, Pradeep K. Effect of welding parameters on microstructure and mechanical properties of friction stir welded joints of AA7039 aluminum alloy. Mater Des 2012;36:379–90. https://doi.org/10.1016/j.matdes.2011.10.054.

[21] Biradar R, Patil S. A systematic review on microhardness, tensile, wear and microstructural properties of aluminum matrix composite joints obtained by friction stir welding: past, present and its future. Trans Indian Inst Met 2024;77: 1923–37. https://doi.org/10.1007/s12666-024-03303-1.

[22] Giorgi M, Scialpi A, Panella FW, Filippis LAC. Effect of shoulder geometry on residual stress and fatigue properties of AA6082 FSW joints. J Mech Sci Technol 2019;23:26–35. https://doi.org/10.1007/s12206-008-1006-4.

[23] Chenghang Z, Guangjie H, Deyin Z, Zhengqi S, Qing L. Microstructure and mechanical properties in dissimilar friction stir welded AA2024/7075 joints at high heat input: effect of post-weld heat treatment. J Mater Res Technol 2020;9(6): 14771–82. https://doi.org/10.1016/j.jmrt.2020.10.053.

[24] Fratini L, Buffa G, Shivpuri R. Mechanical and metallurgical effects of in process cooling during friction stir welding of AA7075-T6 butt joints. Acta Mater 2010;58: 2056–67. https://doi.org/10.1016/j.actamat.2009.11.048.

[25] Dermani OK, Abbasi A, Roeen GA, Nayyeri MJ. Dissimilar friction stir lap welding of AA7075 to AZ31B in the presence of Sn interlayer. Journal of manufacturing process 2021;68:616–31. https://doi.org/10.1016/j.jmapro.2021.05.068.

[26] Vijaya P, Madhusudhan G, Srinivasa K. Microstructure, mechanical and corrosion behavior of high strength AA7075 aluminium alloy friction stir welds, Effect of post weld heat treatment. Def Technol 2015;11:362–9. https://doi.org/10.1016/j.dt.2015.04.003.

[27] Hasan MJ, Mehran TE, Amir C, Reza K, Razieh Y. An artificial neural network model for multi-pass tool pin varying FSW of AA5086-H34 plates reinforced with Al_2O_3 nanoparticles and optimization for tool design insight. CIRP J Manuf Sci Technol 2021;35:69–79. https://doi.org/10.1016/j.cirpj.2021.05.007.

[28] Elangovana K, Balasubramanian V. Influences of tool pin profile and welding speed on the formation of friction stir processing zone in AA2219 aluminium alloy. Journal of material processing and technology 2008;200:163–75. https://doi.org/10.1016/j.jmatprotec.2007.09.019.

[29] Amit G, Ramesh KG. Selection of FSW tool parameters for joining Al-Mg4.2 alloy: an experimental approach. Metallography, microstructure and analysis 2018;7: 524–32. https://doi.org/10.1007/s13632-018-0468-8.

[30] Jayaseelan P, Christy TV, Vijay SJ, Nelson R. Effect of tool material, profile and D/d ratio in friction stir welding of aluminium metal matrix composites. Mater Res Express 2019;6:096590. https://doi.org/10.1088/2053-1591/ab30b1.

[31] Krasnowski K, Hamilton C, Dymek S. Influence of the tool shape and weld configuration on microstructure and mechanical properties of the Al 6082 alloy FSW joints. Arch Civ Mech Eng 2015;15:133–41. https://doi.org/10.1016/j.acme.2014.02.001.

[32] Pankaj K, Dheerendra KD. Effect of tool geometry in dissimilar Al-Steel friction stir welding. J Manuf Process 2021;68:198–208. https://doi.org/10.1016/j.jmapro.2020.08.007.

[33] Rahul K, Kishor KJ, Anwar AA, Murshid I, Chiranjit S. Comparison of microstructure, texture, and mechanical properties of the SQ and thread pin profile FSW joint of AA6061-T6 with Al_2O_3 particle reinforcement. Mater Today Commun 2022;33:104785. https://doi.org/10.1016/j.mtcomm.2022.104785.

[34] Mohsen B, Mohammad B, Kamran D, Nader P. On the role of pin geometry in microstructure and mechanical properties of AA7075/SiC nano-composite fabricated by friction stir welding technique. Mater Des 2014;53:519–27. https://doi.org/10.1016/j.matdes.2013.07.049.

[35] Srinivas T, Madhusudhan G, Koteswararao SR. Microstructure and mechanical properties of friction stir welded AA7075−T651 aluminum alloy thick plates. Transaction Nonferrous Metals society china 2015;25:1770–8. https://doi.org/10.1016/S1003-6326(15)63782-7.

[36] Yuqing M, Liming K, Yuhua C, Fencheng L, Xing L. Inhomogeneity of microstructure and mechanical properties in the nugget of friction stir welded thick 7075 aluminum alloy joints. Journal of material science and technology 2018;34 (1):228–36. https://doi.org/10.1016/j.jmst.2017.11.039.

[37] Sivaraman P, Nithyanandhan MT, Karthick M, Kirivasan SM, Rajarajan S, Sivanesa M. Analysis of tensile strength of AA 2014 and AA 7075 dissimilar metals using friction stir welding. Material Today proceedings 2021;37:187–92. https://doi.org/10.1016/j.matpr.2020.04.895.

[38] Martin R, Jannik G, Jorge FS. Microstructure and mechanical properties of keyhole repair welds in AA 7075-T651 using refill friction stir spot welding. Material and design 2017;132:283–94. https://doi.org/10.1016/j.matdes.2017.07.013.

[39] Navdeep M, Varun S, Sanjay M, Ankit T. Insights into the microstructure evolution and mechanical behavior of dissimilar friction stir welded joints of additively manufactured AlSi10Mg and conventional 7075-T651 aluminum alloys. Mater Sci Eng 2023;881:145407. https://doi.org/10.1016/j.msea.2023.145407.

[40] Hesam P, Rez J, Vahid F, Gholamreza K, Asal HM, Lucas FM, Matteo P. Processing of Al-Cu-Mg alloy by FSSP: parametric analysis and the effect of cooling environment on microstructure evolution. Mater Lett 2021;308:131157. https://doi.org/10.1016/j.matlet.2021.131157.

[41] Ke Z, Zhenyu L, Bolyu X, Zongyi M. Friction stir welding of carbon nanotubes reinforced Al-Cu-Mg alloy composite plates. J Mater Sci Technol 2017;33:1004–8. https://doi.org/10.1016/j.jmst.2017.01.033.

[42] Abhishek S, Vyas MS, Agam G, Pragya R, Surjya KP, Jinu P. Friction stir lap welding of AA6061 aluminium alloy with a graphene interlayer. Mater Manuf Process 2020;35(3):258–69. https://doi.org/10.1080/10426914.2020.1718694.

[43] Zhang ZW, Liu ZY, Xiao BL, Ni DR, Ma ZY. High efficiency dispersal and strengthening of graphene reinforced aluminum alloy composites fabricated by powder metallurgy combined with friction stir processing. Carbon 2018;135: 215–23. https://doi.org/10.1016/j.carbon.2018.04.029.

[44] Mohammad SM, Mohd RM, Farazila Y, Nukman Y, Zbigniew B, Tetsuo S, Yoshiaki M, Hidetoshi F. Improved mechanical and electrical properties of copper-aluminum joints with highly aligned graphene reinforcement via friction stir spot welding. J Mater Res Technol 2023;24:9203–15. https://doi.org/10.1016/j.jmrt.2023.05.155.

[45] Hesam PSH, Mohammad RJ, Johan MVF, Yong SN, Hamed JA, Gholamreza K. An EBSD study on microstructure and texture development in graphene-reinforced Al–Mg–Si nanocomposites via FSP. J Mater Res Technol 2025;35:685–701. https://doi.org/10.1016/j.jmrt.2024.12.190.

[46] Hesam PJM, Mohammad RJ, Gholamreza K. Friction stir processing of AA6061-T6/graphene nanocomposites: unraveling the influence of tool geometry, rotation, and advancing speed on microstructure and mechanical properties. J Alloys Compd 2024;1002:175400. https://doi.org/10.1016/j.jallcom.2024.175400.

[47] Chenghang Z, Guangjie H, Qing L. Quantitative analysis of grain structure and texture evolution of dissimilar AA2024/7075 joints manufactured by friction stir welding. Material Today communications 2021;26:101920. https://doi.org/10.1016/j.mtcomm.2020.101920.

[48] Ratnesh K, Gaurav K, Abhijit R, Ravi SS, Mozammil SM, Prakash O, Asim A. A comparative analysis of friction stir and tungsten inert gas dissimilar AA5082-AA7075 butt welds. Mater Sci Energy Technol 2022;5:74–80. https://doi.org/10.1016/j.mset.2021.12.002.

[49] Mohamed MZA, Mohamed S, Zeinab A, Zidan R, Ramadan M, Sabbah A, Naser A. Microstructure and mechanical properties of dissimilar friction stir welded AA2024-T4/AA7075-T6 T-butt joints. Metals 2021;11:128. https://doi.org/10.3390/met11010128.

[50] Sachinkumar P, Narendranath S, Chakradhar D. Microstructure, Hardness and Tensile properties of friction stir welded aluminum matrix composite reinforced with SiC and Fly Ash. Silicon 2019;11:2557–65. https://doi.org/10.1007/s12633-018-00445.

[51] Arcari A, Dowling NE. Modeling mean stress relaxation in variable amplitude loading for 7075-T6511 and 7249-T76511 high strength aluminum alloys. Int J Fatig 2012;42:238–47. https://doi.org/10.1016/j.ijfatigue.2011.10.016.

[52] Sharma A, Dwivedi V. Effects due to tool design during FSW process of aluminium alloy AA7075-T6. Advances in materials and processing technologies 2022;8: 1510–32. https://doi.org/10.1080/2374068X.2021.1946336.

[53] Tariq M, Khan I, Hussain G, Farooq U. Microstructure and micro-hardness analysis of friction stir welded bi-layered laminated aluminum sheets. Int J Lightweight Mater Manuf 2019;2:123–30. https://doi.org/10.1016/j.ijlmm.2019.04.010.

[54] Aditya M, Nagumothu K, Mahesh T, Prakash S. Effect of heat treatment on the microstructure and mechanical properties of rotary friction welded AA7075 and AA5083 dissimilar joint. Materials 2023;16(6):2464. https://doi.org/10.3390/ma16062464.

[55] Sun ZC, Wu HL, Cao J, Yin ZK. Modeling of continuous dynamic recrystallization of Al-Zn-Cu-Mg alloy during hot deformation based on the internal-state-variable (ISV) method. Int J Plast 2018;106:73–87. https://doi.org/10.1016/j.ijplas.2018.03.002.

[56] Saurabh D, Avik M, Mahapatra D, Satish VK, Chattopadhyay K. Multi-layer graphene reinforced aluminum– Manufacturing of high strength composite by friction stir alloying. Composites Part B 2018;136:63–71. https://doi.org/10.1016/j.compositesb.2017.10.028.

[57] Wu T, Liu Y, Ji S, et al. Refill friction stir spot welding of a graphene-reinforced AA 6061 aluminum alloy. JOM 2025;77. https://doi.org/10.1007/s11837-025-07133-4. 1280–129.

[58] Omkar M, Palkamapally P, Surjya K, Prakash S. TEM analysis and molecular dynamics simulation of graphene coated Al-Cu micro joints. Carbon Trends 2022;9: 100223. https://doi.org/10.1016/j.cartre.2022.100223.

[59] Huijie Z, Baoxin Z, Qiuzhi G, Jianling S, Guoliang H. A review on microstructures and properties of graphene-reinforced aluminum matrix composites fabricated by friction stir processing. J Manuf Process 2021;68:126–35. https://doi.org/10.1016/j.jmapro.2021.07.023.

[60] Xingyu B, Conglin H, Guobing W, Guo L, Hao C, Bin L. Good strength-plasticity compatibility of GNP/AZ31 composites fabricated by FSP: microstructural evolution and mechanical properties. J Mater Res Technol 2022;20:3995–4007. https://doi.org/10.1016/j.jmrt.2022.08.043.

[61] Majid A, Morteza D, Hwan G, Dong K. Investigation of Fe-rich fragments in aluminum-steel friction stir welds via simultaneous Transmission Kikuchi Diffraction and EDS. Acta Mater 2016;117:262–9. https://doi.org/10.1016/j.actamat.2016.06.064.

[62] Shuai W, Xiao W, Jijin X, Jie H, Xuefeng S, Chun Y, Junmei C, Xiaoqi C, Hao L. Strengthening and toughening mechanisms in refilled friction stir spot welding of AA2014 aluminum alloy reinforced by graphene nanosheets. Mater Des 2022;186: 108212. https://doi.org/10.1016/j.matdes.2019.108212.

[63] Khodabakhshi F, Nosko M, Gerlich AP. Effects of graphene nano-platelets (GNPs) on the microstructural characteristics and textural development of an Al-Mg alloy during friction stir processing. Surface and coating technology 2018;335:288–305. https://doi.org/10.1016/j.surfcoat.2017.12.045.

[64] Shuai Z, Gaoqiang C, Jinquan W, Yijun L, Ruishan X, Qu L, Shenbo Z, Gong Z, Qingyu S. Effects of energy input during friction stir processing on microstructures and mechanical properties of aluminum/carbon nanotubes nanocomposites. J Alloys Compd 2019;798:523–30. https://doi.org/10.1016/j.jallcom.2019.05.269.

[65] Lu YJ, Liu QL, Liu YD, Yu C, Chen HX, Chen YX, Liu YJ. Mechanical property and fracture characteristics of carbon fiber reinforced aluminum matrix composites prepared by friction stir welding. J Mater Res Technol 2025;34:1080–9. https://doi.org/10.1016/j.jmrt.2024.12.108.

[66] Abhishek S, Vyas MS, Jinu P. A comparative study on microstructural evolution and surface properties of graphene/CNT reinforced Al6061−SiC hybrid surface composite fabricated via friction stir processing. Trans Nonferrous Met Soc China 2019;29:2005–26. https://doi.org/10.1016/S1003-6326(19)65108-3.

[67] Jessica JL, Malcolm BW, Timothy WR, Matthew PC, Ayanjeet G, Christopher SG, Jordon JB, Gregory BT, Paul GA. A solid-state additive manufacturing method for aluminum-graphene nanoplatelet composites. Materialia 2022;23:101440. https://doi.org/10.1016/j.mtla.2022.101440.

[68] Ajay P, Madhu HC, Abhishek P, Chandra SP, Satish VK, Uma G, Pradeep R. Friction stir processing of squeeze cast A356 with surface compacted graphene nanoplatelets (GNPs) for the synthesis of metal matrix composites. Mater Sci Eng 2019. https://doi.org/10.1016/j.msea.2019.138517.

[69] Krishna KM, Kumar A. Influence of ridges shoulder with polygonal pins on material flow and friction stir weld characteristics of 6082 aluminum alloy. J Manuf Process 2018;32:625–34. https://doi.org/10.1016/j.jmapro.2018.03.034.

[70] Ming Z, Chuansong W, Lei S, Gaoqiang C, Qing S. Dislocation strain energy based modelling for ultrasonic effect on friction stir lap welding process of dissimilar Mg/Al alloys. J Mater Res Technol 2023;22:252–68. https://doi.org/10.1016/j.jmrt.2022.11.133.

[71] Sachinkumar, Narendranath S, Chakradhar D. Characterization and evaluation of joint properties of FSWed AA6061/SiC/FA hybrid AMCs using different tool pin profiles. Transaction of indian institute of metals 2020;73:2269–79. https://doi.org/10.1007/s12666-020-02035-2.

[72] Rajeev K, Jujhar S, Shubham S, Changhe L, Grzegorz K, Szymon W. Neutrosophic entropy-based ingenious measurement for fast fourier transforms based classification of process-parameters and wear resistance of friction-stir processed hybrid AA7075 - B4C aluminium metal-matrix composites. J Mater Res Technol 2022;20:720–39. https://doi.org/10.1016/j.jmrt.2022.07.026.

[73] Xiao L, Hrishikesh D, Mayur P, Lei L, Ayoub S, Glenn JG, Darrell RH, Mert E. Exceptional strength and wear resistance in an AA7075/TiB_2 composite fabricated via friction consolidation. Mater Des 2024;242:113006. https://doi.org/10.1016/j.matdes.2024.113006.

[74] Zhou Z, Jiang Z, Zheng Q, Li Y, Yuan Z, Ding C, Piao Z. Research on the construction of gradient nanostructure and anti-tribo corrosion behavior of aluminum alloy surface. Tribol Int 2024;194:109448. https://doi.org/10.1016/j.triboint.2024.109448.

[75] Prakash KS, Sudesh S, Gaoqiang C, Liu Y, Shuai Z, Qingyu S. Wear behavior of the friction stir alloyed AZ31 Mg at different volume fractions of Al particles reinforcement and its enhanced quality attributes. Tribol Int 2020;146:106268. https://doi.org/10.1016/j.triboint.2020.106268.